High-performance Microelectronic-integratable Molecular Transistors

Yu Xie,[1#] Zhou Cao,[1,2#] Ziming Zhou,[1#] Enrique del Barco,[3] Wenkun Lv,[1] Shuangan Zang,[1] Ningyue Chen,[1] Jin-Liang Lin,[1] Pierre-André Cazade,[4*] Damien Thompson[4*] and Yuan Li[1*]

[1] *Key Laboratory of Organic Optoelectronics and Molecular Engineering and Laboratory of Flexible Electronics Technology, Department of Chemistry, Tsinghua University, Beijing, 100084, P. R. China*

[2] *Quantum Science Center of Guangdong-Hong Kong-Macao Greater Bay Area (Guangdong), Shenzhen, 518000, P. R. China.*

[3] *Department of Physics, University of Central Florida, Orlando, Florida 32816, USA.*

[4] *Department of Physics, Bernal Institute, University of Limerick, Limerick V94 T9PX, Ireland.*

Corresponding authors*

yuanli_thu@tsinghua.edu.cn, damien.thompson@ul.ie, Pierre.Cazade@ul.ie

# These authors contributed equally

Contents

Supplementary Note 1. Chemical synthesis

General procedures: All chemicals were purchased from commercial suppliers and used without further purification (General-reagent®, Bidepharm and Merck). Column chromatography was conducted using chromatographic column (SEPAFLASHTM E, irregular silica, 40-63 μm, 60 Å) purchased from Santai Technologies, Inc. NMR spectra were recorded on a Bruker AVANCE III 400M NMR Spectrometer. Mass spectra of compounds were determined on SHIMADZU LCMS IT/TOF Mass Spectrometer.

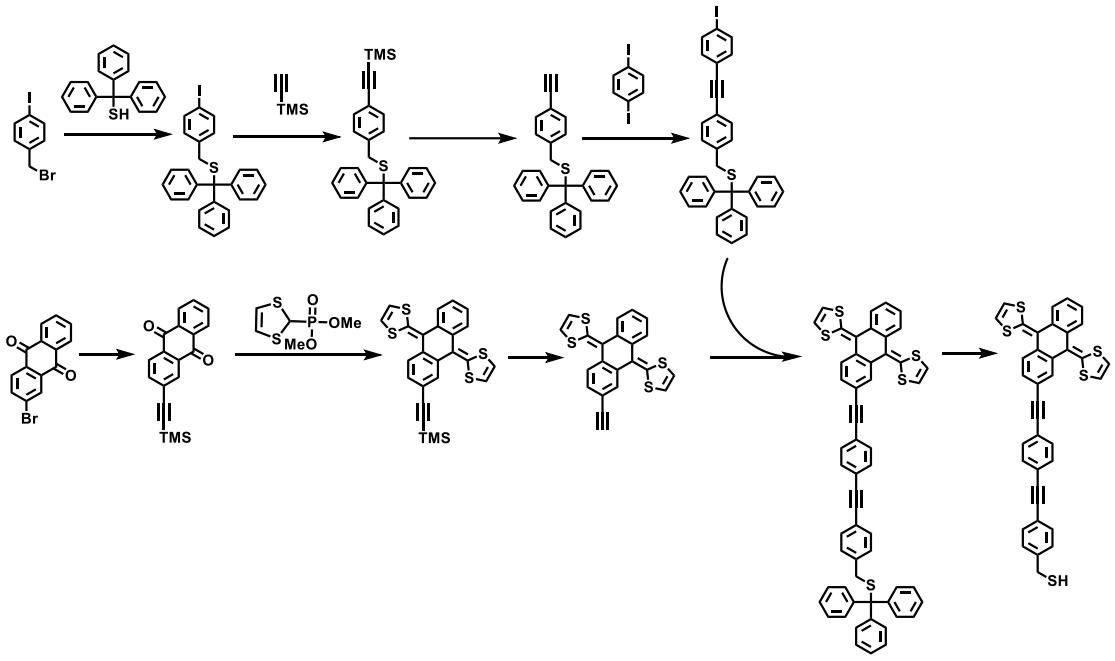

Supplementary Fig. 1 The synthetic route to exTTF-SH.

The synthesis of exTTF-SH was performed following previous reported procedures[1].

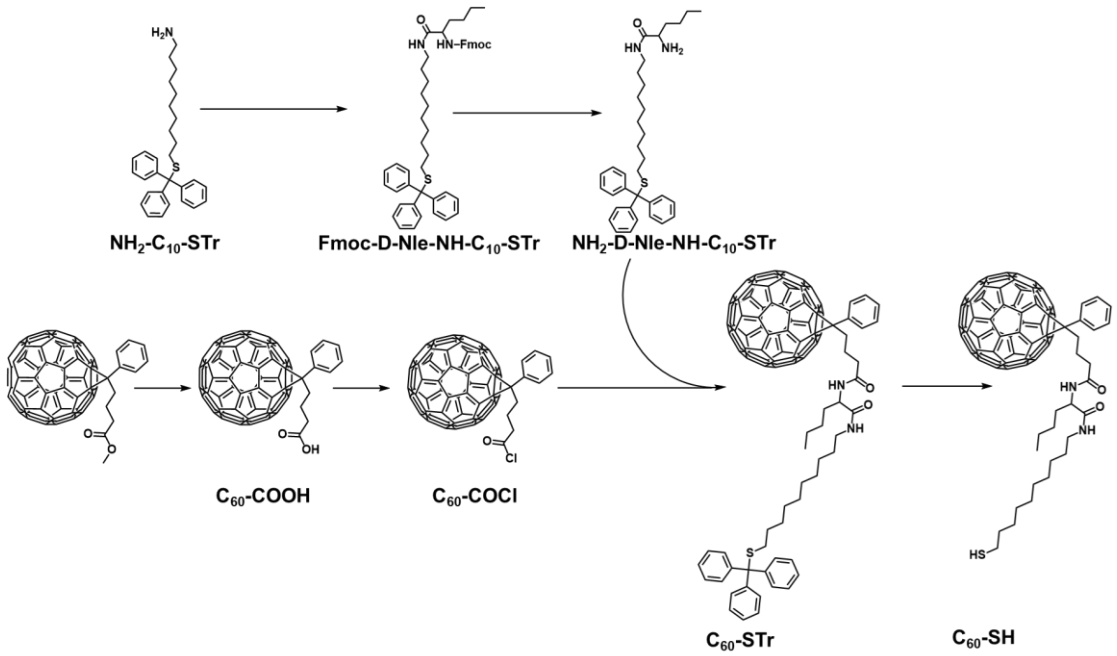

Supplementary Fig. 2 The synthetic route to C_{60}-SH.

The synthesis of **NH_2-C_{10}-STr** followed previously reported methods[2].

Fmoc-D-Nle-NH-C_{10}-STr: In a 250 mL round-bottom flask placed in an ice-water bath, Fmoc-D-Nle-OH (9.19 g, 26 mmol), N, N-diisopropylethylamine (10.08 g, 78 mmol), and HATU (9.89 g, 26 mmol) were dissolved in 180 mL of dichloromethane. The mixture was stirred for 30 minutes, after which NH_2-C_{10}-STr (9.77 g, 22.6 mmol) was added, and the reaction was allowed to proceed at room temperature for 8 hours. The reaction mixture was then washed sequentially with 100 mL of 8% NaH_2PO_4 aqueous solution, 100 mL of 10% $NaHCO_3$ solution, and 100 mL of water. The organic phase was dried over anhydrous $MgSO_4$, and the solvent was removed under reduced pressure using a rotary evaporator. The crude product was purified by column chromatography (silica gel, ethyl acetate/petroleum ether = 1:4 v/v) to yield a pure white solid. Yield: 12.67 g, 73%. ^{1}H NMR (400 MHz, $CDCl_3$): 7.76 (d, J = 7.5 Hz, 2H), 7.58 (d, J = 7.5 Hz, 2H), 7.45 – 7.36 (m, 8H), 7.32 (d, J = 7.4 Hz, 2H), 7.30 – 7.25 (m, 6H), 7.23 – 7.17 (m, 3H), 4.40 (d, J = 7.2 Hz, 2H), 4.21 (t, J = 6.9 Hz, 1H), 4.06 (d, J = 7.5 Hz, 1H),

3.29 – 3.18 (m, 2H), 2.12 (t, J = 7.3 Hz, 2H), 1.49 – 1.09 (m, 24H), 0.89 (t, J = 4.4 Hz, 3H). ^{13}C NMR (101 MHz, $CDCl_3$): 145.22, 141.46, 129.75, 127.93, 127.89, 127.23, 126.64, 125.18, 120.15, 66.49, 47.32, 39.72, 32.59, 32.16, 29.64, 29.56, 29.47, 29.35, 29.29, 29.14, 28.73, 27.75, 26.98, 22.56, 14.07. MS (MALDI-TOF, DHB) m/z $[M+Na]^+$ found: 789.7124.

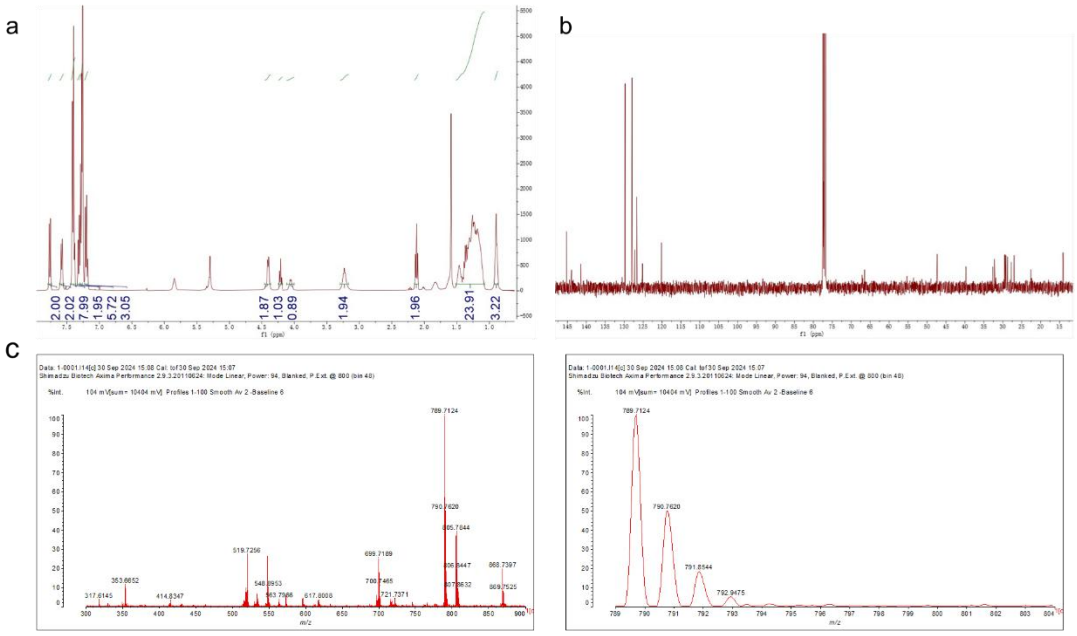

Supplementary Fig. 3 (a) ^{1}H NMR, (b) ^{13}C NMR and (c) MALDI-TOF-MS spectra of Fmoc-D-Nle-NH-C_{10}-STr.

NH_2-D-Nle-NH-C_{10}-STr: In a 250 mL round-bottom flask, Fmoc-D-Nle-NH-C_{10}-STr (12.50 g, 16.3 mmol) was combined with acetonitrile (160 mL) and diethylamine (16 mL). The reaction mixture was stirred at room temperature for 1 hour, after which the solvent was removed under reduced pressure. The crude product was purified by column chromatography (silica gel, methanol/dichloromethane = 1:50 v/v) to yield a pure yellow oil, which solidified into a white solid upon freezing. Yield: 7.62 g, 86%. ^{1}H NMR (400 MHz, $CDCl_3$): 7.43-7.39 (m, 6H), 7.31-7.24 (m, 6H), 7.23-7.17 (m, 3H), 3.34 (dd, J = 4.31, 8.22 Hz, 1H), 3.23 (dt, J = 6.16, 8.14 Hz, 2H), 2.13 (t, J = 7.31 Hz, 2H), 1.55-1.43 (m, 3H), 1.11-1.41 (m, 22H), 0.95-0.88 (m, 3H). ^{13}C NMR (101 MHz,

$CDCl_3$): 175.06, 145.21, 129.73, 127.92, 126.62, 77.48, 77.36, 77.16, 76.84, 66.48, 55.39, 53.56, 39.12, 38.74, 34.99, 32.15, 29.77, 29.55, 29.45, 29.38, 29.28, 29.12, 28.71, 28.13, 27.05, 22.69, 14.13. MS (MALDI-TOF, DHB) m/z $[M+Na]^+$ found: 567.7399.

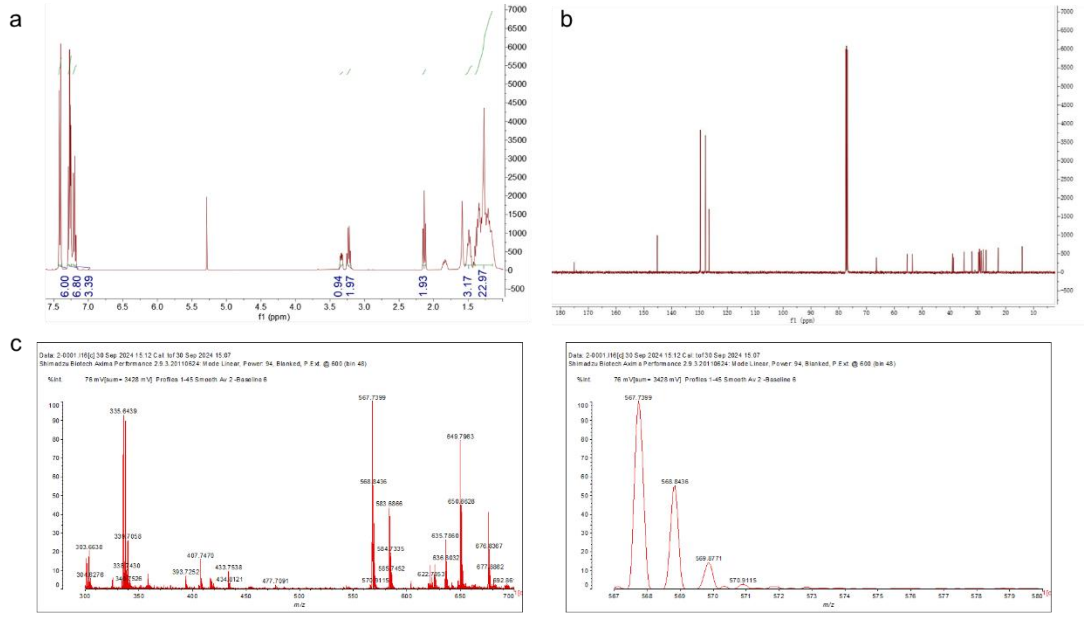

Supplementary Fig. 4. (a) ^1H NMR, (b) ^{13}C NMR and (c) MALDI-TOF-MS spectra of NH_2-D-Nle-NH-C_{10}-STr.

C_{60}-COOH: In a three-neck round bottom flask, 500 mg PCBM (0.55 mmol) was dissolved in 100 ml of anhydrous toluene. 100 ml glacial acetic and 30 ml concentrated hydrochloric acid were added into the solution. After refluxing at 100 ℃ for 36 h under nitrogen atmosphere, the solution was cooled to room temperature and filtered. The crude solid was rinsed with toluene, water and acetone. The dark brown product was dried in vacuo under 50 ℃ and can be used without further purification. The NMR spectrum could not be reliably recorded due to the poor solubility of the compound.

C_{60}-COCl: In a three-neck round bottom flask, 100 mg C_{60}-COOH (0.11 mmol) was dissolved in 150 ml carbon disulfide (CS_2). The solution was cooled to 0 ℃ and oxalyl chloride was added dropwise. After stirred at 0 ℃ for 1 h, the reaction mixture was

heated to reflux for 20 h under nitrogen atmosphere. The solvent was removed on rotary-evaporator and the fresh product should be used immediately without further purification.

C_{60}-STr: In a three-neck round bottom flask, 150 mg NH_2-D-Nle-NH-C_{10}-STr (0.27 mmol) was dissolved in 20 ml toluene and 30 mg anhydrous triethylamine was added under nitrogen atmosphere. C_{60}-COCl was dissolved in 20 ml toluene and added into flask dropwise. The reaction mixture was stirred for overnight under room temperature. After the removal of solvent, the crude product was purified by column chromatography (silica gel, toluene / ethyl acetate 10:1 as eluent). ^{1}H NMR (400 MHz, $CDCl_3$): 7.92-7.96 (m, 2H), 7.53-7.58 (m, 2H), 7.49 (t, J = 7.4 Hz, 1H), 7.41-7.45 (m, 6H), 7.26-7.32 (m, 6H), 7.20-7.25 (m, 3H), 5.90-6.30 (m, 2H), 4.36 (s, 1H), 3.18-3.32 (m, 2H), 2.88-2.96 (m, 2H), 2.37-2.46 (m, 2H), 2.20-2.27 (m, 2H), 2.15 (t, J = 7.3 Hz, 2H), 1.47-1.56 (m, 2H), 1.15-1.40 (m, 22H), 0.91 (t, J = 6.8 Hz, 3H). ^{13}C NMR (101 MHz, $CDCl_3$): 148.82, 147.81, 145.88, 145.15, 145.10, 144.81, 144.68, 144.52, 144.44, 144.02, 143.78, 143.05, 143.01, 142.95, 142.25, 142.19, 142.13, 141.02, 140.76, 138.06, 137.58, 136.78, 132.12, 129.62, 128.47, 128.28, 127.93, 126.50, 79.95, 77.22, 66.39, 53.31, 51.92, 39.65, 36.26, 33.82, 32.41, 32.05, 29.70, 29.49, 29.44, 29.35, 29.22, 29.18, 29.01, 28.62, 27.69, 26.87, 22.98, 22.50, 13.96. MS (MALDI-TOF, DHB) m/z $[M+Na]^+$ found: 1446.4087.

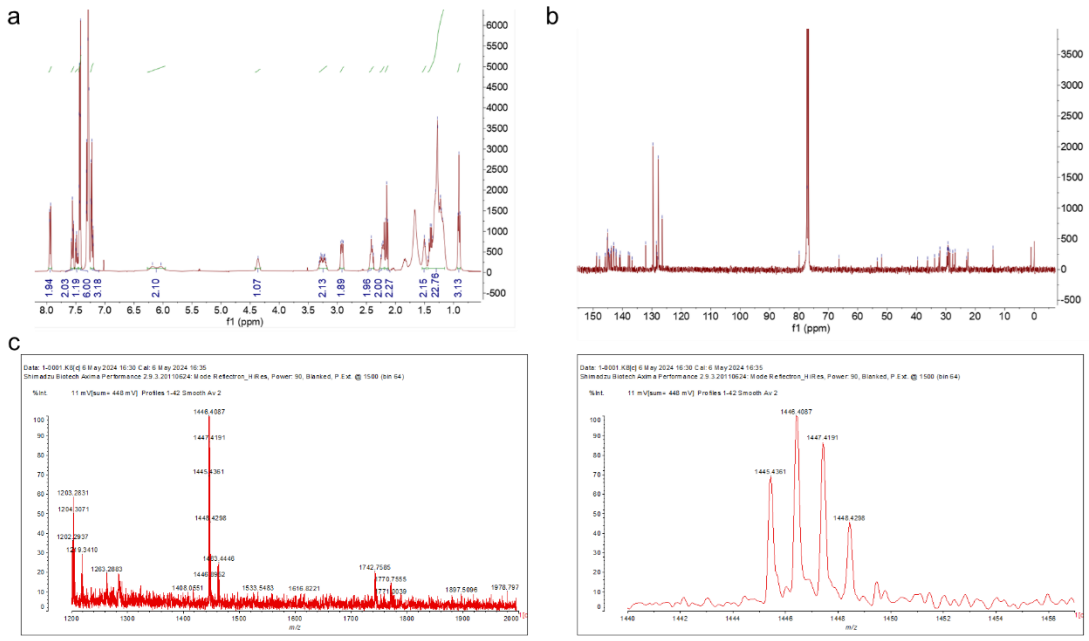

Supplementary Fig. 5 (a) ^{1}H NMR, (b) ^{13}C NMR and (c) MALDI-TOF-MS spectra of C_{60}-STr.

C_{60}-SH: In a three-neck round bottom flask, 50 mg C_{60}-STr (0.042 mmol) was dissolved in 20 ml CS_2 and 200 µl triethylsilane was added under nitrogen atmosphere. 10 ml trifluoroacetic acid was added into flask dropwise and the reaction mixture was stirred for 5 h under room temperature. After quenched with water and extraction with dichloromethane, the solvent was removed and the crude product was purified by column chromatography (silica gel, toluene / ethyl acetate 10:1 as eluent). ^{1}H NMR (400 MHz, $CDCl_3$) δ 7.90-7.98 (m, 2H), 7.53-7.62 (m, 2H), 7.46-7.52 (m, 1H), 5.91-6.23 (m, 2H), 4.32-4.40 (m, 1H), 3.15-3.40 (m, 2H), 2.87-2.98 (m, 2H), 2.50-2.59 (m, 2H), 2.41 (t, J = 7.55 Hz, 2H), 2.16-2.28 (m, 2H), 1.62-1.58 (m, 2H), 1.48-1.55 (m, 2H), 1.25-1.34 (m, 20H), 0.91 (t, J = 6.93 Hz, 3H). ^{13}C NMR (101 MHz, $CDCl_3$) δ 171.49, 148.82, 147.82, 145.88, 145.21, 145.16, 145.08, 145.06, 144.81, 144.77, 144.71, 144.68, 144.53, 144.45, 144.03, 143.78, 143.12, 143.05, 143.01, 142.96, 142.94, 142.25, 142.19,

142.15, 142.13, 141.02, 140.77, 138.06, 137.58, 136.78, 132.12, 128.47, 128.28, 79.94, 77.21, 53.31, 51.92, 39.64, 36.26, 34.02, 33.82, 32.40, 29.49, 29.45, 29.43, 29.21, 29.04, 28.36, 27.69, 26.86, 24.65, 22.97, 22.50,13.96. MS (MALDI-TOF, DHB) m/z $[M+Na]^+$ found: 1203.9857.

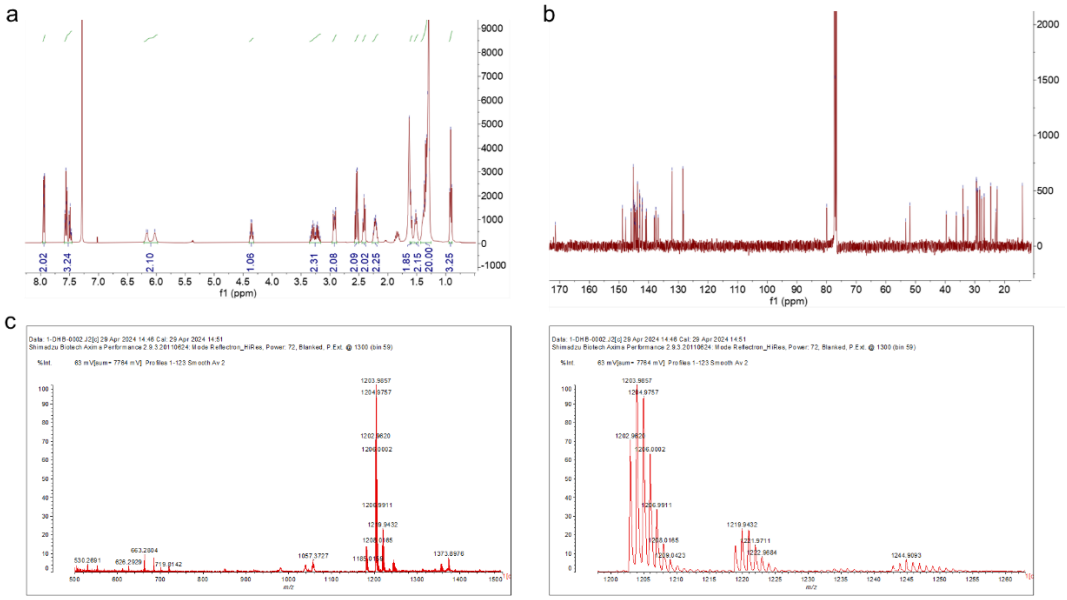

Supplementary Fig. 6 (a) ^{1}H NMR, (b) ^{13}C NMR and (c) MALDI-TOF-MS spectra of C_{60}-SH.

Supplementary Note 2. Comparison with state-of-art molecular transistors and integrated functional molecular devices

We conducted a literature survey to compare our molecular transistors with reported single molecular transistors (SMT) and self-assembled monolayer transistors (SAMT). Supplementary Table 1 compiles the functional groups, ON/OFF ratio, working temperature, dielectric materials, architecture and features of corresponding molecular transistors, linked to Figure 3j in main text.

Supplementary Table 1. Comparison with state-of-art molecular transistors

Molecules	**SMT or SAMT**	**ON/OFF ratio**	**Working temperature (K)**	**Dielectric materials**	**Architecture**	**Features**	**Reference**
exTTF, C_{60}	SAMT	10^3-10^4	R.T.*-350	Ionic liquid	Vertical	High performance at and above room temperature, logic gates implementation, wafer-scale integration	This work

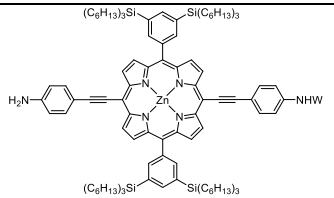 Zinc-porphyrins	SMT	10^3-10^5	10-100	HfO_2	Planar	Quantum interference SMT	3
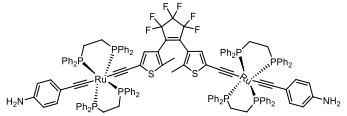 $H_2N–C_6H_4–C≡C(dppe)_2Ru$	SMT	10^3	80	HfO_2/Al_2O_3	Planar	Ru-DAE dual gate SMT	4
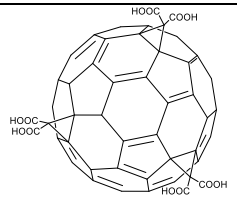 Carboxyfullerene	SAMT	30	77	TiO_2/Al_2O_3	Vertical	Quantum dot SAMT	5

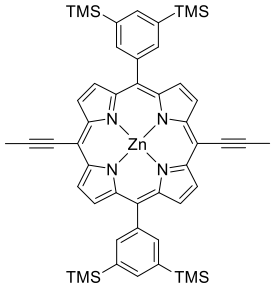 Zinc-porphyrins	SMT	19.2	77	SiO_2	Planar	Coulomb-blockage SMT	6
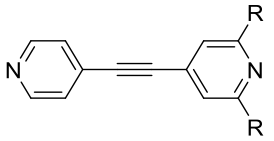	SAMT	3.16	300	Ionic liquid	Vertical	OPT SAMT	7
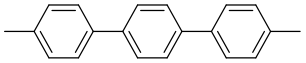	SMT	10	R.T.	Ionic liquid	Planar	Aromatic-ring SMT	8
Bovine serum albumin (BSA) protein	SAMT	133	R.T.	TiO_2	Vertical	Single-layer protein SAMT	9
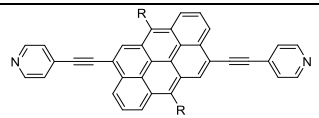	SAMT	306	R.T.	Ionic liquid	Vertical	Quantum interference SAMT	10

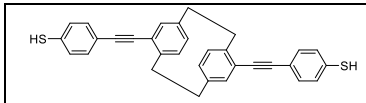	SAMT	330	R.T.	Ionic liquid	Vertical	Quantum interference SAMT	11
$Co_6E_8L_6$ cluster	SMT	600	R.T.	-	Vertical	Single-cluster SMT	12
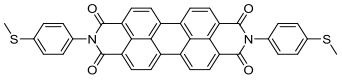 PTCDI	SMT	1000	R.T.	$NaClO_4$ solution	Vertical	PTCDI SMT	13
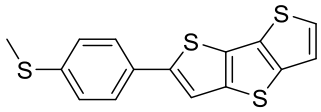 TPCOs	SMT	1300	R.T.	Electrolyte	Vertical	Supramolecular SMT	14
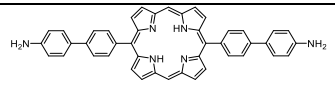 porphyrins	SMT	4800	R.T.	Ionic liquid	Planar	Proton transfer SMT	15

*R.T. stands for room temperature.

We conducted a literature study to compare our integrated molecular transistors with other integrated functional molecular devices, including molecular transistors, diodes, memories. Supplementary Table 2 compiles the integration, yield, architecture and functions of integrated molecular devices, linked to Figure 5f in main text.

Supplementary Table 2. Comparison with integrated functional molecular devices

Techniques	Integration	Yield (%)	Architecture	Functions	Reference
Graphene wet transfer	~8000	>90%	Vertical	Molecular transistors	This work
Ionic liquid gating	1,000*	22	Planar	Molecular transistors	8
EGaIn stamping	100	93	Vertical	Molecular diodes	16
EGaIn microfluidic	10	80	Vertical	Molecular diodes	17
Carbon nanotube	16	100	Vertical	Molecular memories	18
EGaIn microfluidic	10	60	Vertical	Molecular memories	19
Silicon nanowire	160,000	31	Vertical	Molecular memories	20

* Estimated value from images of the device.

Supplementary Note 3. Experimental methods

Supplementary Note 3.1 Device fabrication

The schematic fabrication flow of molecular transistors is depicted in Supplementary Fig. 7. The SLG used in this work is characterized through Raman spectrum to ensure its high quality (Fig.S6a). Supplementary Fig. 8b shows optical microscopy image of Al_2O_3 micropore, whose sectional profile was measured through AFM (Oxford Cypher VRS), showing the height of 30 nm (Supplementary Fig. 8c). The surface roughness of Au is 1.0 nm (Supplementary Fig. 8d). Process variations were subjected to statistical analysis. AFM measurements of 38 pores across 9 devices yielded an area distribution of 21.78 ± 1.02 μm², corresponding to a 4.7% variation (Supplementary Fig. 8e), which indicates a minimal impact on the accuracy of current distribution. Both AFM and TEM revealed a gentle slope exceeding 100 nm at the pore edges resulting from wet etching. This feature renders the exact pore height non-critical and enables the graphene to form complete, continuous coverage. EDS characterization showed no or only background-level Al signal inside the pores (Supplementary Fig. 8f). Consistent surface roughness measurements from AFM further confirmed sufficient etching of the alumina. The ionic liquid [DEME]+[TFSI]$^-$ is purchased from Merck and the corresponding chemical structure is depicted in Supplementary Fig. 9.

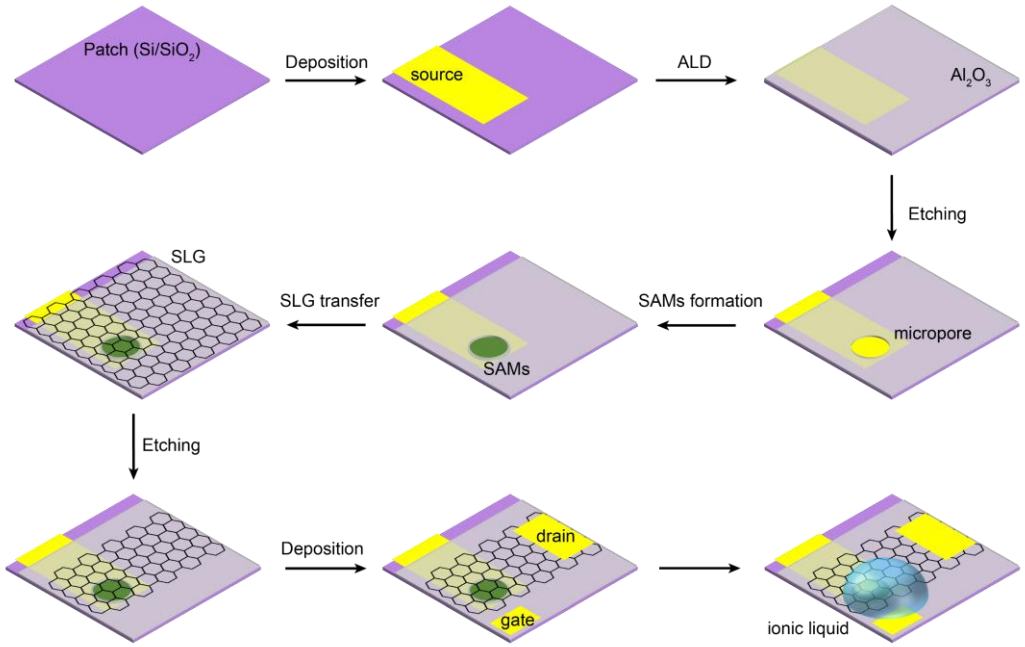

Supplementary Fig. 7 Device fabrication flow of molecular transistors.

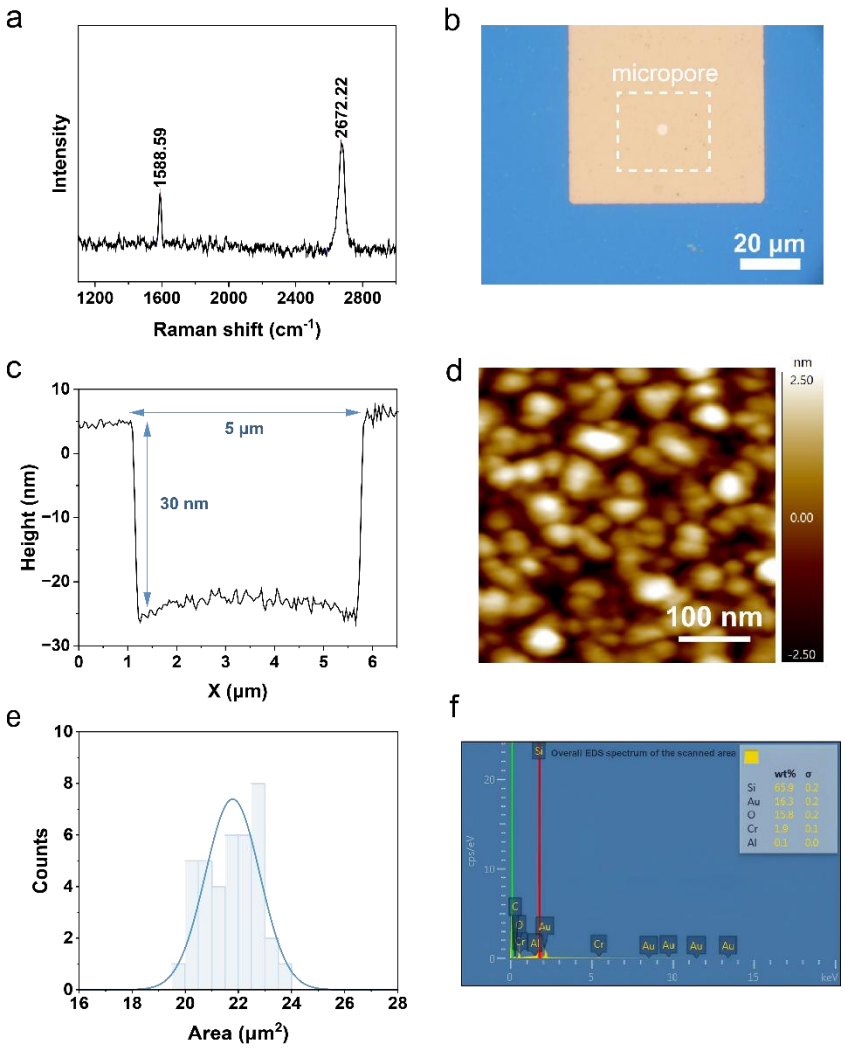

Supplementary Fig. 8 a. Raman spectrum of single-layer graphene. b. Optical image of Al_2O_3 micropore on Au pad. c. Section profile of Al_2O_3 micropore recorded by AFM. d. AFM image of Au substrate with surface roughness of 1.0 nm. e. The area of Al_2O_3 pores obtained by AFM exhibits a normal distribution with a mean of 21.78 ± 1.02 μm². f. Overall EDS spectrum within the Al_2O_3 pore show an elemental statistical proportion of 0.1 wt%, consistent with the background, while the non-etched area exhibits 2 wt%.

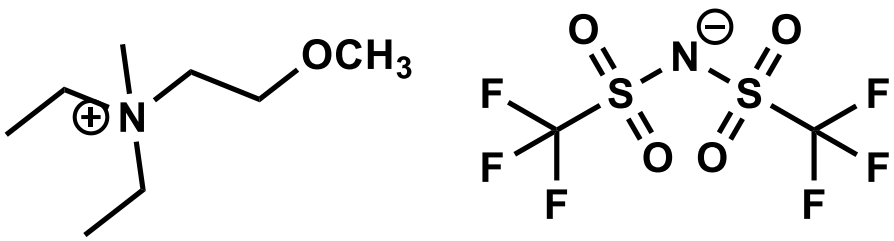

Supplementary Fig 9. The chemical structure of ionic liquid $[DEME]^+[TFSI]^-$.

Supplementary Note 3.2 Sample preparation for STEM

The schematic procedures to prepare samples for STEM are depicted in Supplementary Fig. 10. Supplementary Fig. 11a demonstrates the STEM images of slab cutting around the Al_2O_3 micropore. The edges of Al_2O_3 micropore are not that steep due to the isotropic etching of Al_2O_3 through BOE. The EDS analysis of Au elements confirms the presence of an additional Au layer deposited on the molecular junctions. (Supplementary Fig. 11).

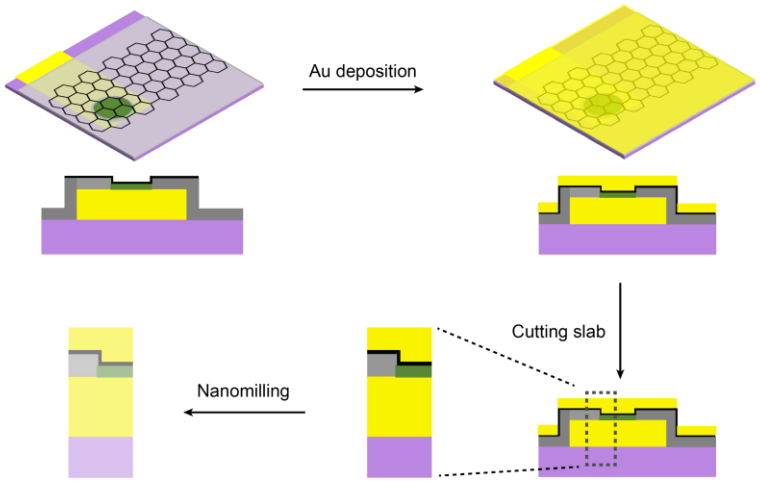

Supplementary Fig. 10 The procedures to prepare the FIB sample.

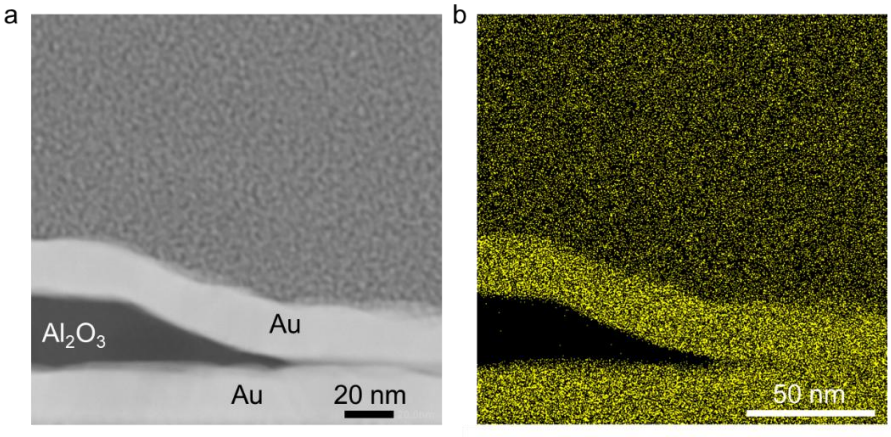

Supplementary Fig. 11 (a) The STEM images of slab cutting around the Al_2O_3 micropore. (b) The Energy-dispersive X-ray spectroscopy (EDS) analysis of Au.

Supplementary Note 3.3 Photoelectron spectroscopy

XPS and UPS was carried out with ESCALAB Xi+ (Thermo Fisher Scientific CN) in NCESBJ (Beijing) and in an ultrahigh vacuum chamber with pressure of 10^{-8} Pa. To probe the valence band, the photon energy of 21.22 eV was used and -9.62 V bias was applied to the sample to overcome the work function of the analyzer. According to the fitting of S 2*p* doublet with binding energy (B.E.) at ~162.0 eV, thiols form covalent Au-S bonds to the gold bottom electrodes. As for Au-S-exTTF, another S 2*p* doublet with binding energy at 163.5 eV and more intense signal, suggests that thiophene groups are on the head of the SAMs (Supplementary Fig. 12)[1].

The thickness and surface coverage of the monolayers can be calculated by

$$\frac{I_{\mathrm{C}(1s)}}{I_{\mathrm{Au}(4f)}} = k\frac{1-e^{-d_{\mathrm{C}}/\lambda_{\mathrm{C}}}}{e^{-d_{\mathrm{CS}}/\lambda_{\mathrm{Au}}}}$$

where I is the integrated peak area, λ_C is the escape depth of C 1*s* photoelectrons through the carbon layer, λ_{Au} is the escape depth of the Au 4*f* photoelectrons through the thiolate layer, d_C is the thickness of the carbon layer, and d_{CS} is the thickness of the thiolate layer, and k is an instrument-specific constant. To calibrate the instrument, the C_{1s}/Au_{4f} intensity ratios of all samples were calculated and compared with the corresponding ratio for SC_{18} -SAMs of known thickness[21] so as to obtain the thickness of all samples. Once the thickness d was obtained, the surface coverage could be derived. The relative surface coverage Γ_{SAM} was estimated by comparing the attenuated Au 4*f* signals of SAMs with different anchoring groups, using the expression:

$$I_{0,\mathrm{Au}} = \frac{I_{\mathrm{Au}}}{e^{-d/\lambda}}$$

Here, $I_{0,\mathrm{Au}}$ denotes the hypothetical Au 4*f* signal in the absence of attenuation by the

SAM. The measured surface coverage of SC18 on Au has been reported as 6.94×10^{-10} mol cm^{-2}[21]. Therefore, by comparing the $I_{0,\mathrm{Au}}$ values of all SAMs with that of SC_{18} on Au, the corresponding Γ_{SAM} values for the SAMs in this study were estimated.

UPS was used to determine the HOMO level of molecules in SAMs. Supplementary Fig. 13 shows the HOMO onset edge and secondary electron peak of the UPS spectra. HOMO is calculated through equation 1 (hv = 21.22 eV).

$$E_{HOMO} = E_{cutoff} - E_{onset} - hv \quad (1)$$

The SAM work function (WF) is also calculated from the UPS spectrum and by the following equation:

$$WF = hv - E_{cutoff} \quad (2)$$

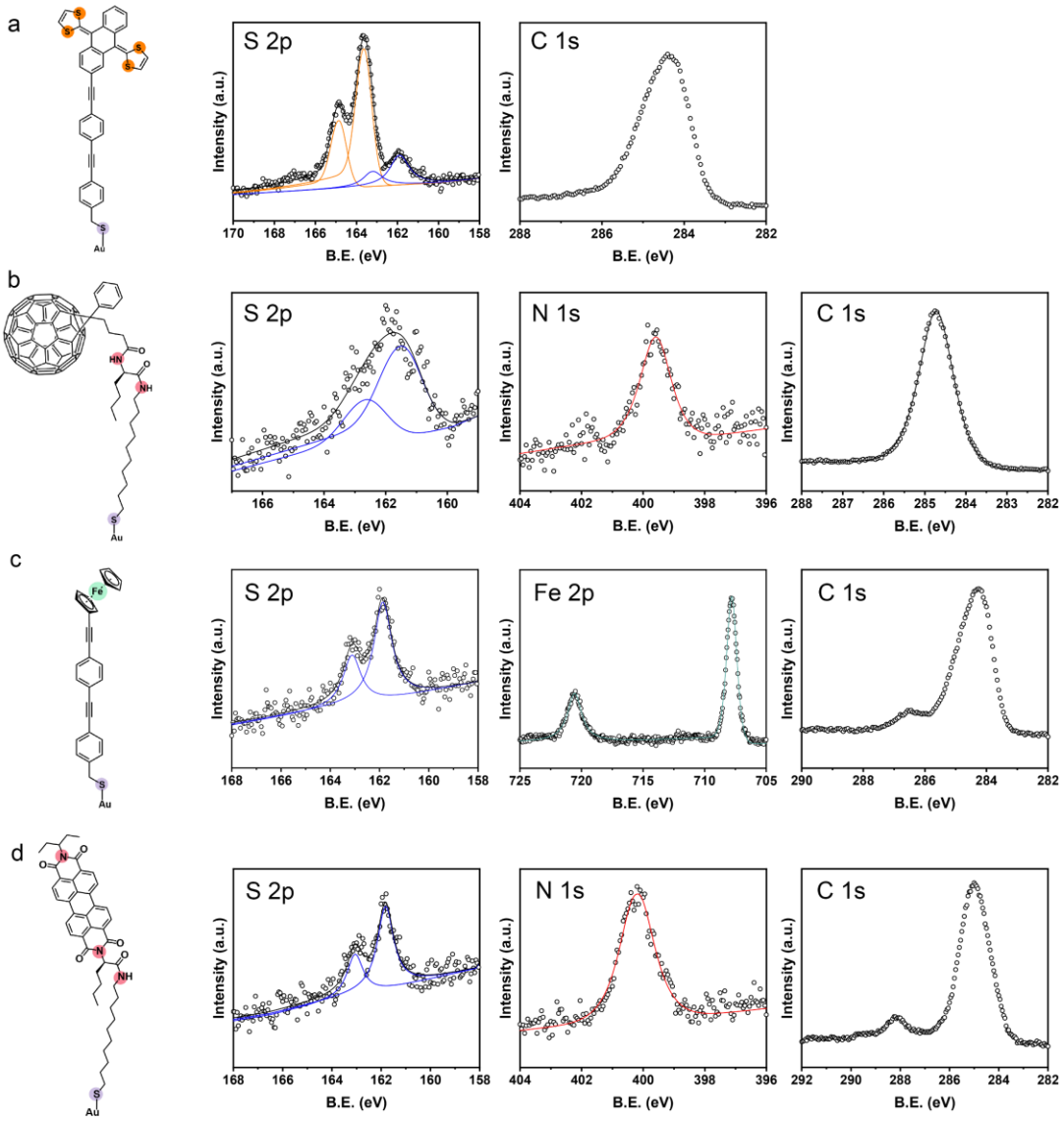

Supplementary Fig. 12 S 2*p*, C 1*s*, N 1*s* and Fe 2*p* regions of XPS spectra for SAMs derived from (a) exTTF-SH. (b) C_{60}-SH, (c) Fc-SH and (d) PDI-SH on Au substrates.

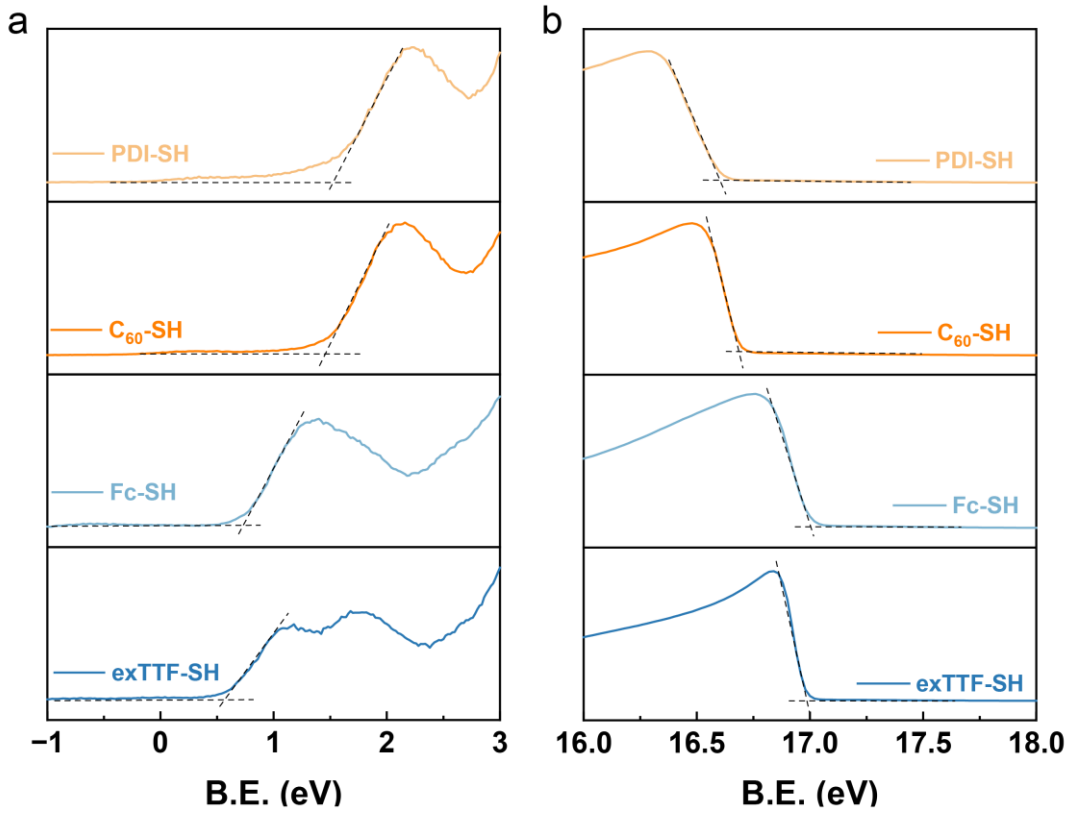

Supplementary Fig. 13 Detailed region of (a) HOMO onset and (b) secondary electron cutoff of UPS spectra for SAMs on Au substrates.

Supplementary Note 3.4 UV-vis absorption spectra

UV-vis absorption spectra of solutions were carried out with concentration of ~ 0.1 mmol L^{-1} in toluene with UV-vis spectrometer (Agilent 8453). According to previous research[22], HOMO-LUMO gap (E_g, eV) of molecules and E_{LUMO} can be determined through equation:

$$E_g = 1240/\lambda_{onset} \quad (3)$$

$$E_{LUMO} = E_{HOMO} + E_g \quad (4)$$

In the equation, λ_{onset} is the onset wavelength of UV-vis absorption spectra (Supplementary Fig. 14).

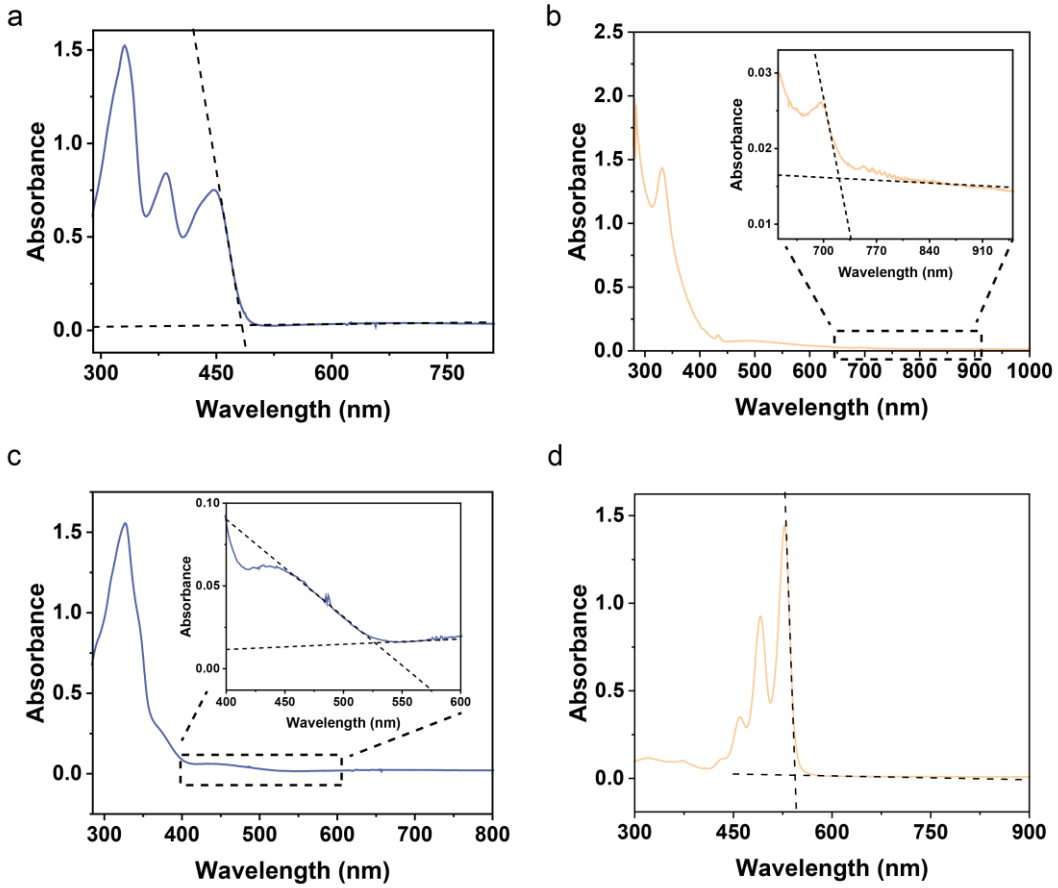

Supplementary Fig. 14 The UV-vis absorption spectra of (a) exTTF-SH, (b) C_{60}-SH, (c) Fc-SH and (d) PDI-SH in toluene, with concentration of ~ 0.1 mmol L^{-1}. The insets in panel b and c show the detailed plots, determining the onset wavelength according to the previous research[23,24].

Supplementary Table 3. Energy levels of SAMs

SAMs	HOMO (eV)	LUMO (eV)	E_g (eV)	Onset wavelength (nm)
exTTF-SH	-4.91	-2.34	2.57	483.25
C_{60}-SH	-6.05	-4.33	1.72	720.52
Fc-SH	-4.97	-2.62	2.35	526.81
PDI-SH	-6.23	-3.95	2.28	543.78

Supplementary Note 3.5 Additional characterization of SAMs

Supplementary Table 4. Thickness and coverage of SAMs

SAMs	Thickness(Å) (ellipsometer)	Thickness(Å) (XPS)	Surface coverage (1×10^{-10} mol/cm^2)
exTTF-SH	24.4±2.1	23.9	6.74
C_{60}-SH	25.0±0.6	24.6	5.29
Fc-SH	24.0±1.3	23.2	6.82
PDI-SH	23.1±0.8	23.3	6.49
C18-SH[21]		23.3	6.94

Supplementary Table 5. Water contact angle of SAMs

SAMs	Water contact angle(°)
exTTF-SH	69.2±1.8
C_{60}-SH	94.1±1.1
Fc-SH	77.8±1.3

PDI-SH	76.3±1.5

Supplementary Note 3.6 On-chip combination of HOMO- and LUMO-type molecular junctions

We used a simple method to fabricate on-chip combination of HOMO- and LUMO-type molecular junctions, in order to realize NOT gate. Half of the as-fabricated patch was immersed into exTTF-SH solution for one day and washed with corresponding solvent to form the HOMO-type SAMs. Then we reversed the patch to immerse the other half into C_{60}-SH solution to form the LUMO-type SAMs on the same patch.

Supplementary Note 4. Charge transport in molecular transistors

Supplementary Note 4.1 Two-terminal molecular junctions

To characterize the asymmetric behavior of Au-S-exTTF//SLG and Au-S-C_{60}//SLG two-terminal molecular junctions, Supplementary Fig. 15 presents the current density distributions for Au-S-exTTF//SLG at V_{ds} = ± 1.0 V and Au-S-C_{60}//SLG at V_{ds} = ± 1.5 V. The current density distributions exhibit distinct discrete peaks under reverse bias conditions. Furthermore, the ratio distributions of current densities between opposite bias polarities are presented in Supplementary Fig. 15c and 15d.

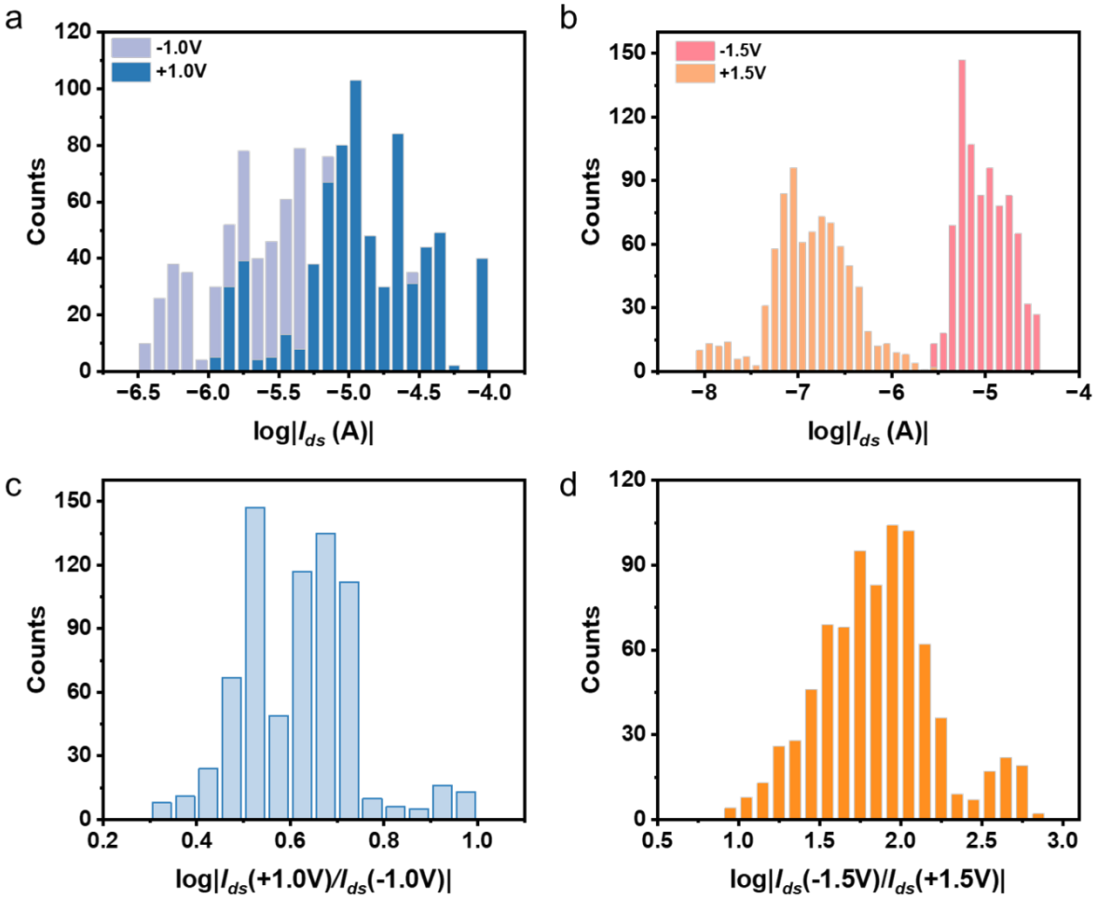

Supplementary Fig. 15 Distribution of current density for (a) Au-S-exTTF//SLG at V_{ds} = ± 1.0 V and (b) Au-S-C_{60}//SLG at V_{ds} = ± 1.5 V. The distribution of ratio between current density under reverse bias polarities for (c) Au-S-exTTF//SLG and (d) Au-S-C_{60}//SLG.

Temperature-dependent measurements were carried out on Au-S-exTTF//SLG two-terminal junctions (Fig.S14), Au-S-C_{60}//SLG two-terminal junctions (Supplementary Fig. 17) and Au-SC_{18}//SLG two-terminal junctions (Supplementary Fig. 18), to demonstrate the respective charge transport mechanisms for the two molecular junctions. The non-linear behavior of the Arrhenius plot in Supplementary Fig. 16b, showing a temperature-dependent (thermally activated) region at high temperatures and a temperature-independent (saturation) region at low temperatures, is a well-documented phenomenon in molecular junctions. This effect was reported in early work by van der Zant et al. (2006) and has been comprehensively explained in the framework of a single-level tunneling model. As detailed by Christian A. Nijhuis and colleagues in their 2016 paper ("A Single-Level Tunnel Model to Account for Electrical Transport through Single Molecule- and Self-Assembled Monolayer-based Junctions"), this behavior can be understood in terms of a broadening of the molecular energy level. At higher temperatures, internal molecular vibrations, excited by the increasing current as the system is brought closer to resonance, broaden the level width, leading to an activated transport process. As the temperature decreases further, this vibration-induced broadening freezes out, and the transport enters a quantum coherent regime where the current becomes temperature-independent. This plateau at low temperatures is a signature of coherent, off-resonant tunneling, consistent with our interpretation.

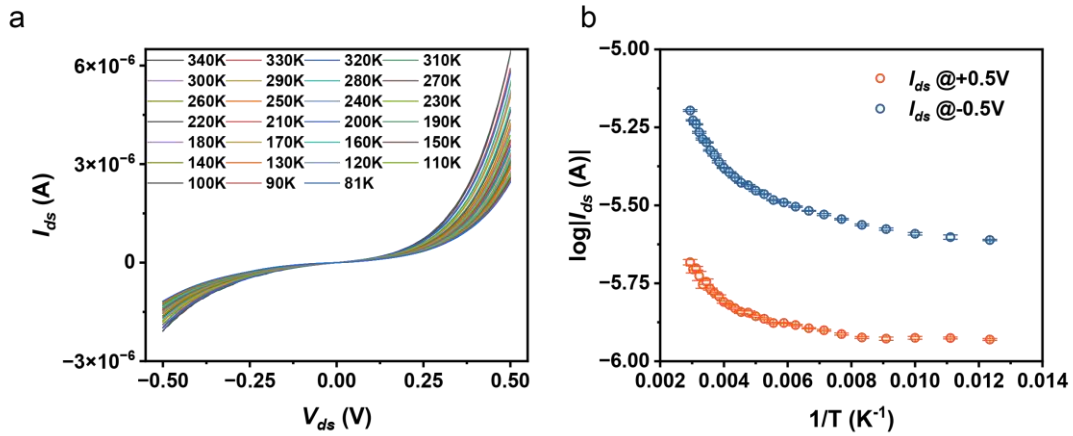

Supplementary Fig. 16 Temperature-dependent measurements I_{ds}-V_{ds} of two-terminal Au-S-exTTF//SLG junctions. (a) Plots of current in linear scale versus bias. (b) log|I_{ds}| under different temperatures at V_{ds} = ± 0.5 V. Error bars represent standard deviation (SD).

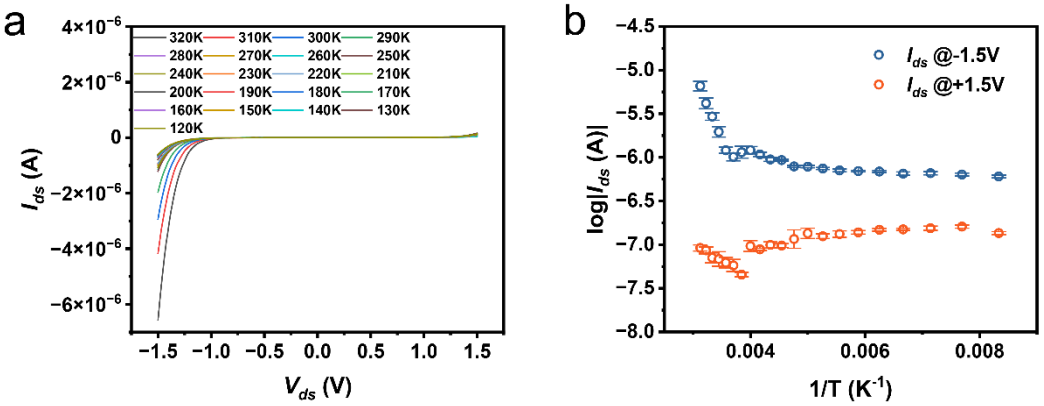

Supplementary Fig. 17 Temperature-dependent measurements I_{ds}-V_{ds} of two-terminal Au-S-C_{60}//SLG junctions. (a) Plots of current in linear scale versus bias. (b) log|I_{ds}| under different temperatures at V_{ds} = ± 1.5 V. Error bars represent standard deviation (SD).

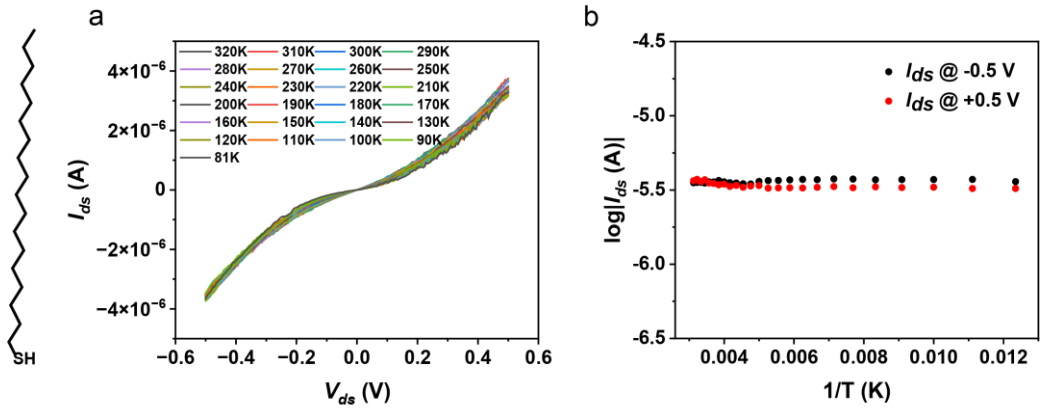

Supplementary Fig. 18 Electrical measurements of 1-octadecanethiol (SC_{18}) based two-terminal molecular junctions Au-SC_{18}//SLG. (a) Plots of current in linear scale versus bias. (b) $\log|I_{ds}|$ under different temperatures at $V_{ds} = \pm 0.5$ V.

Supplementary Note 4.2 Molecular transistors based on exTTF-SH and C_{60}-SH

The transfer characteristics of molecular transistors at $V_{ds} > 0$ are plotted in Supplementary Fig. 19, comprising exTTF-SH and C_{60}-SH, featuring HOMO- and LUMO-type characteristics respectively. Thus, the polarities of V_{ds} are not the determining factors for the type of molecular transistors. We also tested the temperature dependence at $V_{ds} = -0.5$ V and found the results to be largely consistent with those previously obtained at $+0.5$ V. As shown in Supplementary Fig. 20, variations in V_{ds} have only a minor effect on the switching ratio of the molecular field-effect transistor. Similar switching behavior is observed under both bias conditions, although the absolute current levels differ. The transfer characteristics for high performance molecular transistors with ON/OFF near 10^4 comprising exTTF-SH and C_{60}-SH are demonstrated in Supplementary Fig. 21 and Supplementary Fig. 22.

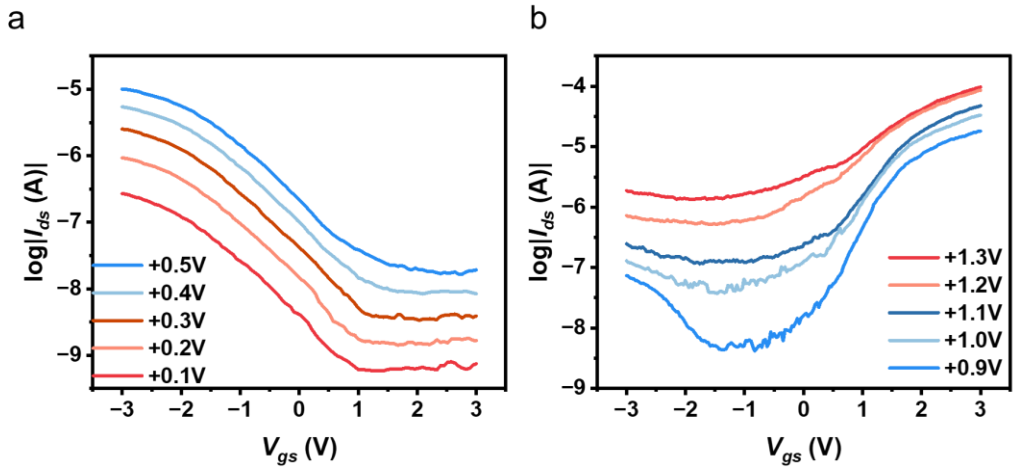

Supplementary Fig. 19 The transfer characteristics of molecular transistors at $V_{ds} > 0$, comprising exTTF-SH and C_{60}-SH.

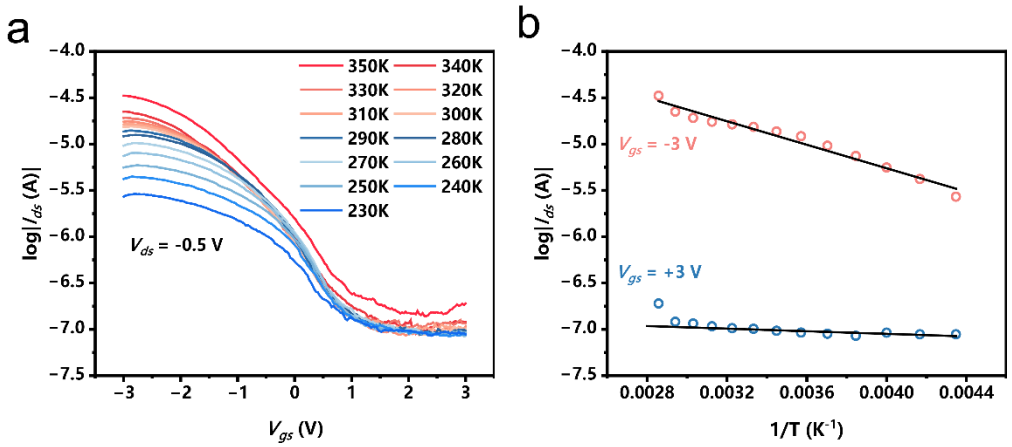

Supplementary Fig. 20 a. The temperature-dependent transfer characteristics for HOMO-type transistors at V_{ds} = -0.5 V. b. corresponding Arrhenius plots of log|I_{ds}| at ON and OFF state.

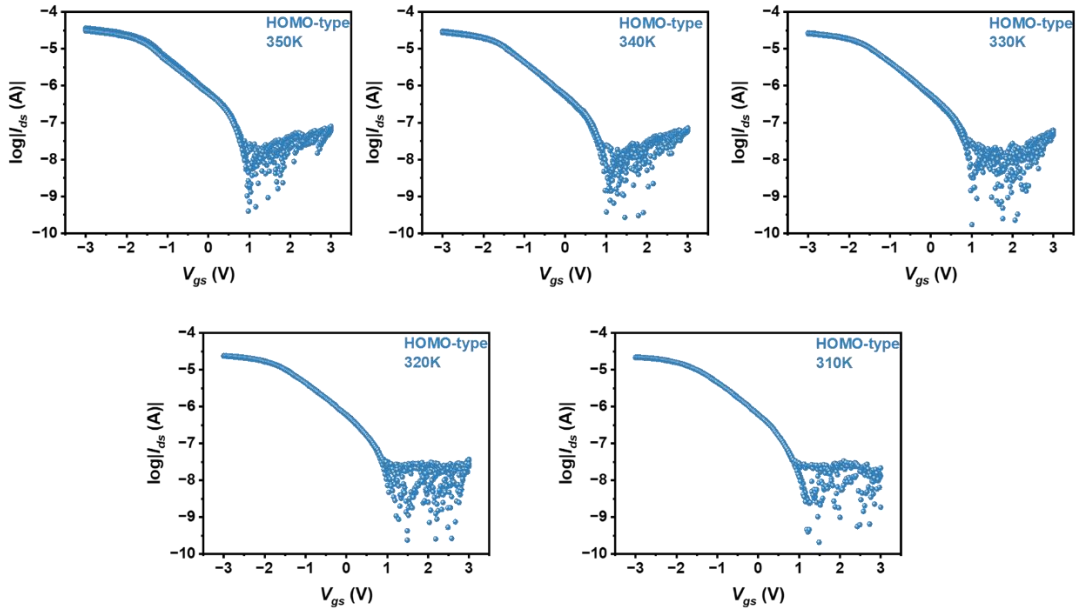

Supplementary Fig. 21 The transfer characteristics for exTTF-SH from 310 to 350 K.

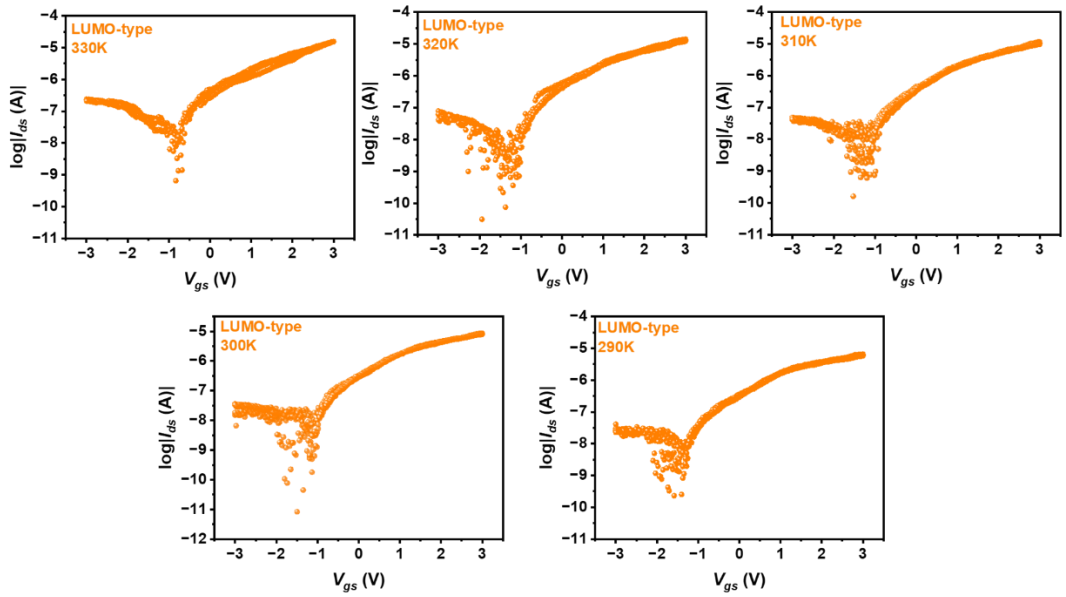

Supplementary Fig. 22 The transfer characteristics for C_{60}-SH from 290 to 330 K.

Supplementary Note 4.3 The Influence of Supramolecular Structures on Molecular Transistors

Molecular junctions developed based on SAMs require consideration not only of the influence of their electronic structure on electrical properties but also of the role of supramolecular structures. Intermolecular interactions affect the density of SAMs, thereby significantly impacting charge transport. As observed in our work, the quality and packing behavior of each molecular SAM significantly influence electrical performance, particularly the off-state current and its stability. Since LUMO-type molecules typically possess extensive conjugated structures, they exhibit poor solubility and aggregation regularity, hindering the growth of dense, ordered SAMs. For instance, in two LUMO-type molecules with same backbones but without side chains, reduced solubility and lower packing density led to a markedly lower switching ratio. (Supplementary Fig. 23)

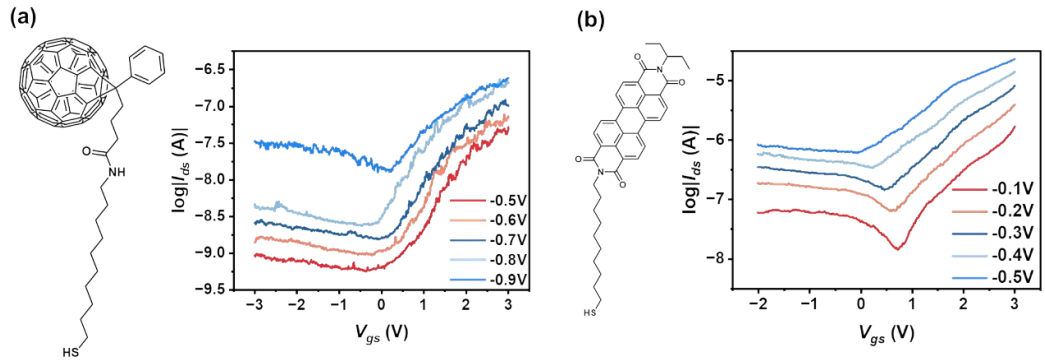

Supplementary Fig. 23 a. Structural diagram of C_{60} molecules without side chains and its measured FET transfer curve diagram. b. Structural diagram of PDI molecules without side chains and its measured FET transfer curve diagram.

Supplementary Note 4.4 Molecular transistors based on ferrocene derivatives and perylene diimides derivatives

To further validate the relationship between electronic structures and the transfer

characteristics of molecular transistors, we incorporated additional molecules, including ferrocene derivatives (Fc-SH) and perylene diimides derivatives (PDI-SH), into the molecular transistors (Supplementary Fig. 24).

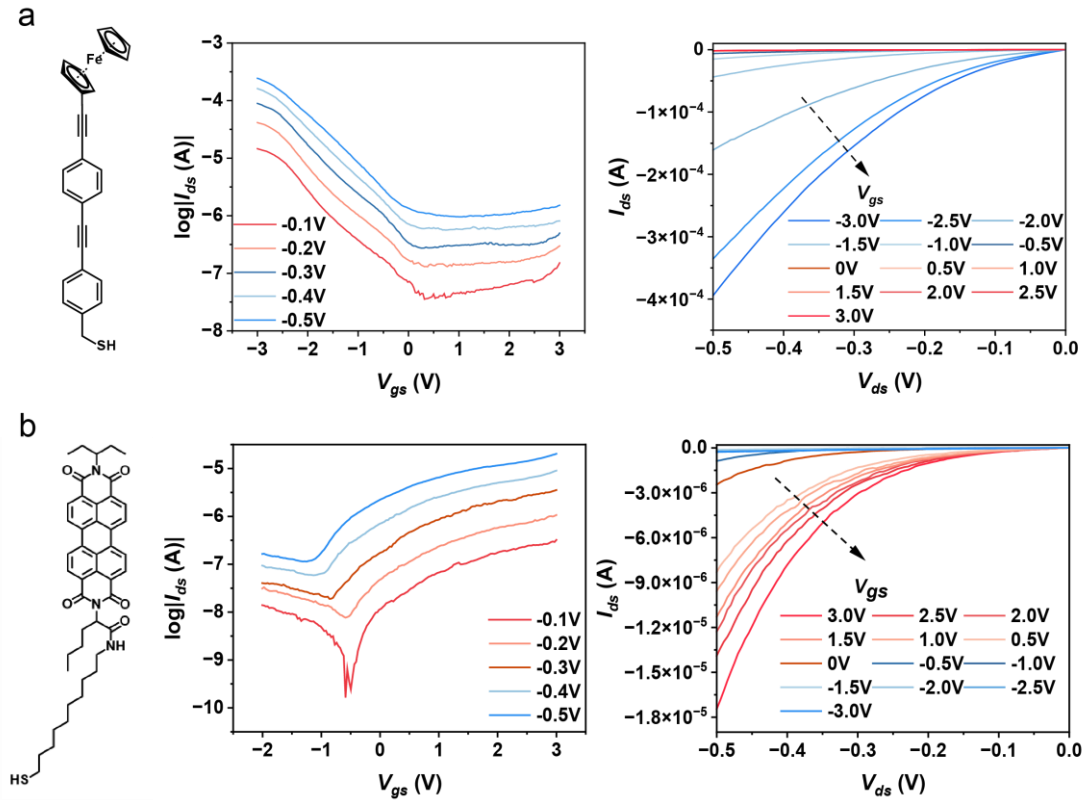

Supplementary Fig. 24 General design strategy for HOMO-type and LUMO-type transistors. (a) Chemical structure of Fc-SH and corresponding transistor performance. (b) Chemical structure of PDI-SH and corresponding transistor performance.

Supplementary Note 4.5 Control experiments for molecular transistors

To elucidate the significance of molecular frontier orbitals in proximity to the E_F of SLG, we performed control experiments using junctions Au-SC_{18}//SLG and Au//SLG. The Au-SC_{18}//SLG junction exhibited weak HOMO-type characteristics (Supplementary Fig. 25). We interpret this finite ratio as arising from two combined effects. First, as observed in previous studies, alkanethiols can induce a weak p-type doping effect on the single-layer graphene (SLG) electrode, which can slightly modulate the overall device current. Second, and more importantly, even though the HOMO and LUMO levels of alkanethiols (C18) are far from the Fermi level of the electrodes, the electric field from the gate, which penetrates through the graphene, can still modulate the molecular energy landscape. As demonstrated in the framework for tunneling transistors by Duan et al. (Sci. Adv., 2018, 4, eaat8237), a positive gate voltage can lower the LUMO, and a negative gate voltage can raise the HOMO. In both cases, this field effect brings one of the molecular orbitals slightly closer to the Fermi level compared to the zero-gate-voltage condition, leading to a small increase in the transmission function and thus a measurable, albeit modest, ON-OFF ratio. Regarding the Au//SLG junction in the absence of SAMs, the output characteristics exhibit linear I_{ds}-V_{ds} behavior, suggesting the formation of an ohmic contact at the Au-SLG interface (Supplementary Fig. 26).

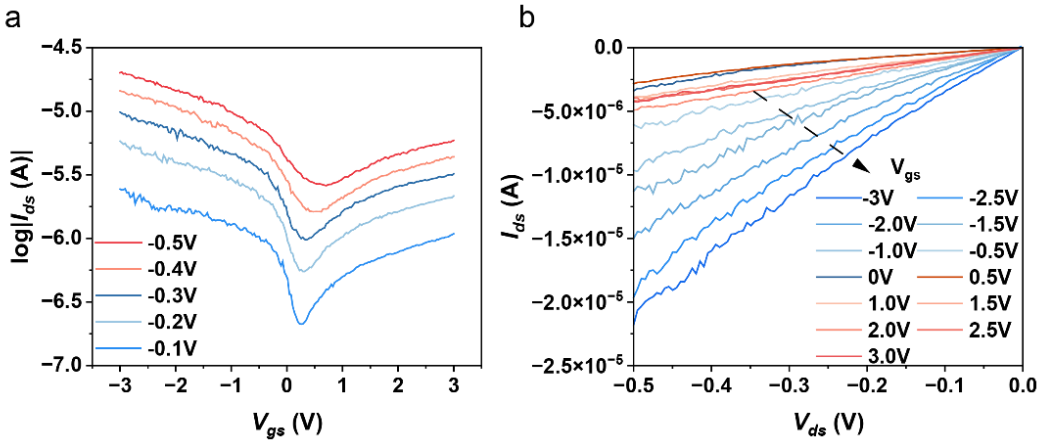

Supplementary Fig. 25 Performance of 1-octadecanethiol (SC_{18}) based molecular transistors. (a) Transfer characteristics and (b) output characteristics of SC_{18}-based transistors. The ON/OFF ratio of SC_{18}-based transistors is around 10 as reported before[11].

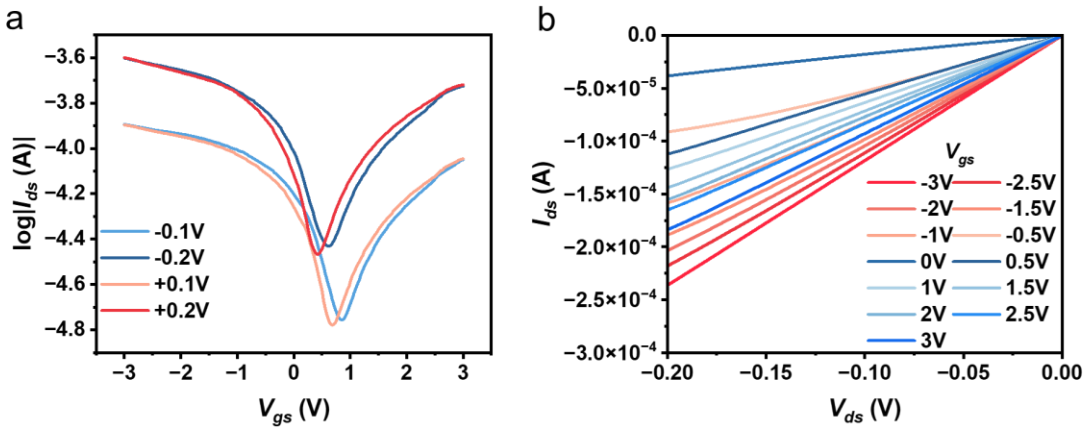

Supplementary Fig. 26 Performance of graphene transistors without SAMs. (a) Transfer characteristics demonstrates the ON/OFF ratio of graphene transistors is around 5. (b) Output characteristic shows the linear I_{ds}-V_{ds} plot.

Supplementary Note 4.6 Other ionic liquids

To confirm that the electrical properties of the molecular transistors are independent of the type of ionic liquid used, we employed two distinct ionic liquids as gate dielectrics to measure the transfer characteristics with V_{ds} = 0.1 V. The transfer characteristics exhibit HOMO-type behavior, demonstrating that the transfer characteristics are independent of the type of ionic liquid used (Supplementary Fig. 27).

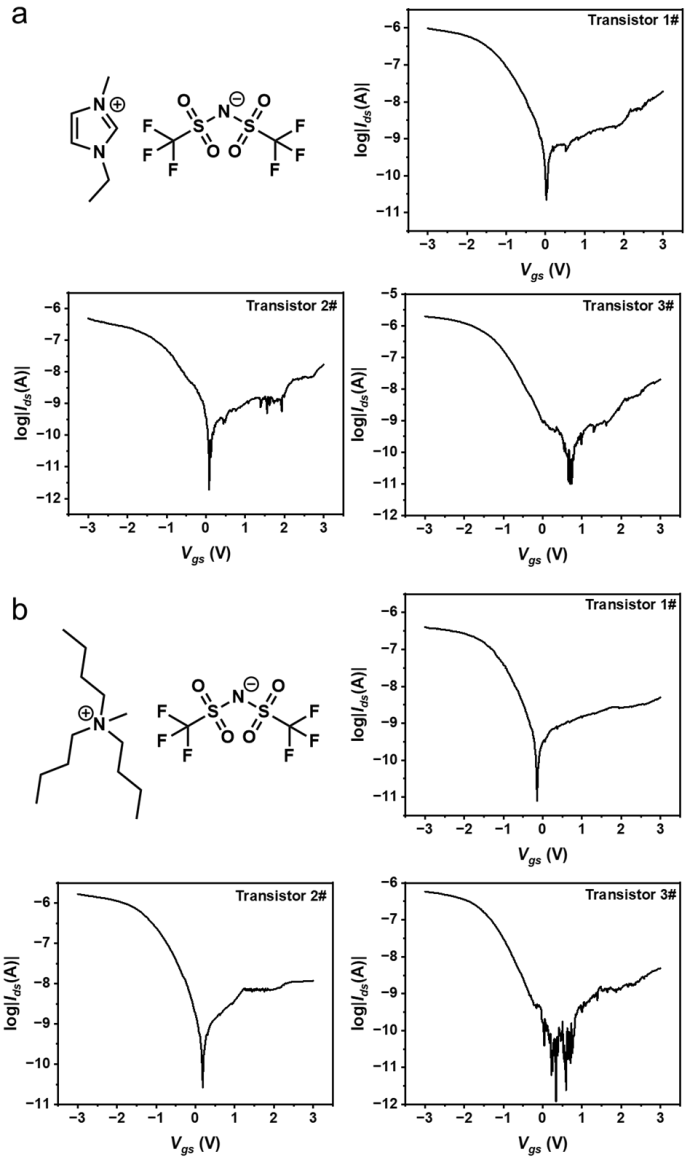

Supplementary Fig. 27 Performance of molecular transistors with other ionic liquid as gate dielectric. Transfer characteristics of exTTF-SH transistors with ionic liquid (a) 1-ethyl-3-methylimidazolium bis(trifluoromethylsulfonyl)imideand and (b) tributylmethylammonium bis(trifluoromethanesulfonyl)imide as gate dielectric.

Supplementary Note 4.7 Electrical measurements of integrated molecular transistors

To streamline the fabrication process for wafer-scale molecular transistors, we initially deposit the source, drain, and gate electrodes. Subsequently, following the deposition of Al_2O_3, we perform etching to selectively expose the corresponding electrodes. We fabricated four patches to conduct electrical measurements of integrated molecular transistors, to analyze the average performance of molecular transistors. We analyzed the proportion of working junctions from four patches and compile it in Supplementary Table 6. During electrical testing, measurements were taken from multiple distinct regions on these wafers, with each region containing 36 transistors and approximately 10 points measured per region. The reported dataset is based on independent measurements across roughly 17 different regions—one of which involved testing all 36 transistors in that region. We performed statistical analysis of the ON/OFF ratios separately for each device. The results show that the distribution of ON/OFF ratios remains consistent across devices #1 to #4 (Supplementary Fig. 28), indicating that our data—drawn from a large number of devices across multiple wafers—exhibits highly repeatable statistical behaviour suitable for mass fabrication. We included 20 representative individual I_{ds}-V_{ds} curves of working junctions from 4 patches in Supplementary Fig. 29. In addition, we included 20 representative individual I_{ds}-V_{gs} curves of HOMO-type transistors from 4 patches in Supplementary Fig. 30. We performed further data processing and analysis, using the ON/OFF ratio as a metric for classifying functional transistor behavior while incorporating calculations and statistics related to subthreshold swing. (Supplementary Fig. 32) From the ON/OFF analysis, transistors with log(ON/OFF) > 3.0 were classified as functional, as values below this threshold deviate significantly from the fitted normal distribution. This switching-ratio criterion gives a functional yield of 84.0%. In parallel, we extracted the subthreshold swing for all transfer curves. To reduce the influence of capacitive spikes on SS extraction, a wider fitting window of 0.375 V was applied. The resulting SS distribution is 767 ± 354 mV/dec. Using $SS < 1000$ mV/dec as the functional threshold, the corresponding yield is 77.6%. Thus, among the originally identified "working" transistors, nearly 77% demonstrate ultrarobust transistor characteristics. Given that the yield of originally identified working transistors is 94.8%, the combined conservative

functional transistor yield is therefore 94.8% × 77% = 73%. Combining both metrics, we confirm a conservative functional transistor yield of 73% for our devices.

Supplementary Table 6. Yield of integrated molecular junctions collected from four different patches

Patch Number	Number of junctions	Working	Yield (%)
1#	25	25	100%
2#	38	34	89.5
3#	80	78	97.5
4#	50	46	92.0
total	193	183	94.8

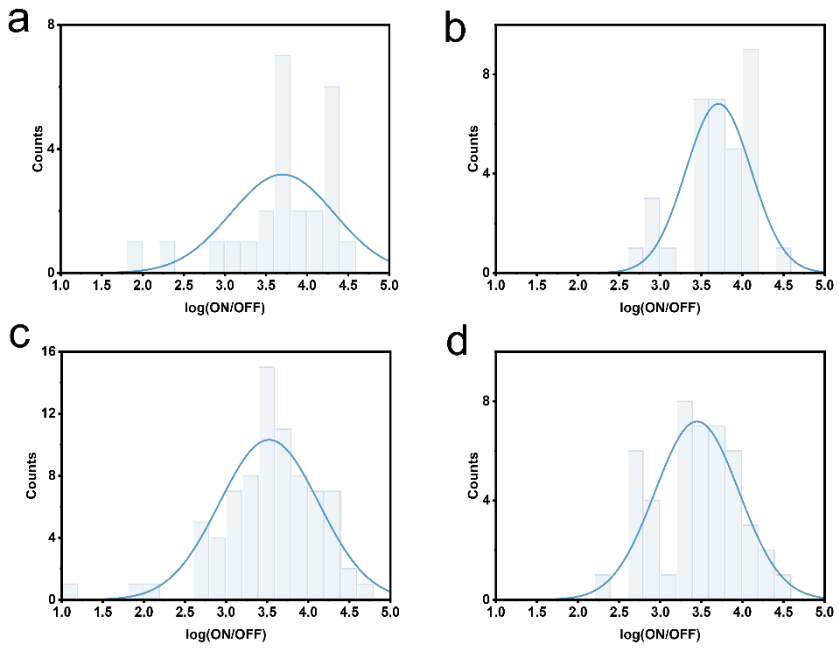

Supplementary Fig. 28 a. Device #1 measured ON/OFF ratio distribution of the transfer characteristic curve, yielding a distribution result of log(ON/OFF) = 3.70 σlog(ON/OFF) = 0.63. a. Device #2 measured ON/OFF ratio distribution, yielding a distribution result of log(ON/OFF) = 3.71 σlog(ON/OFF) = 0.40. c. Device #3 measured ON/OFF ratio distribution, yielding a distribution result of log(ON/OFF) =

3.52 σlog(ON/OFF) = 0.60. d. Device #4 measured ON/OFF ratio distribution, yielding a distribution result of log(ON/OFF) = 3.44 σlog(ON/OFF) = 0.51.

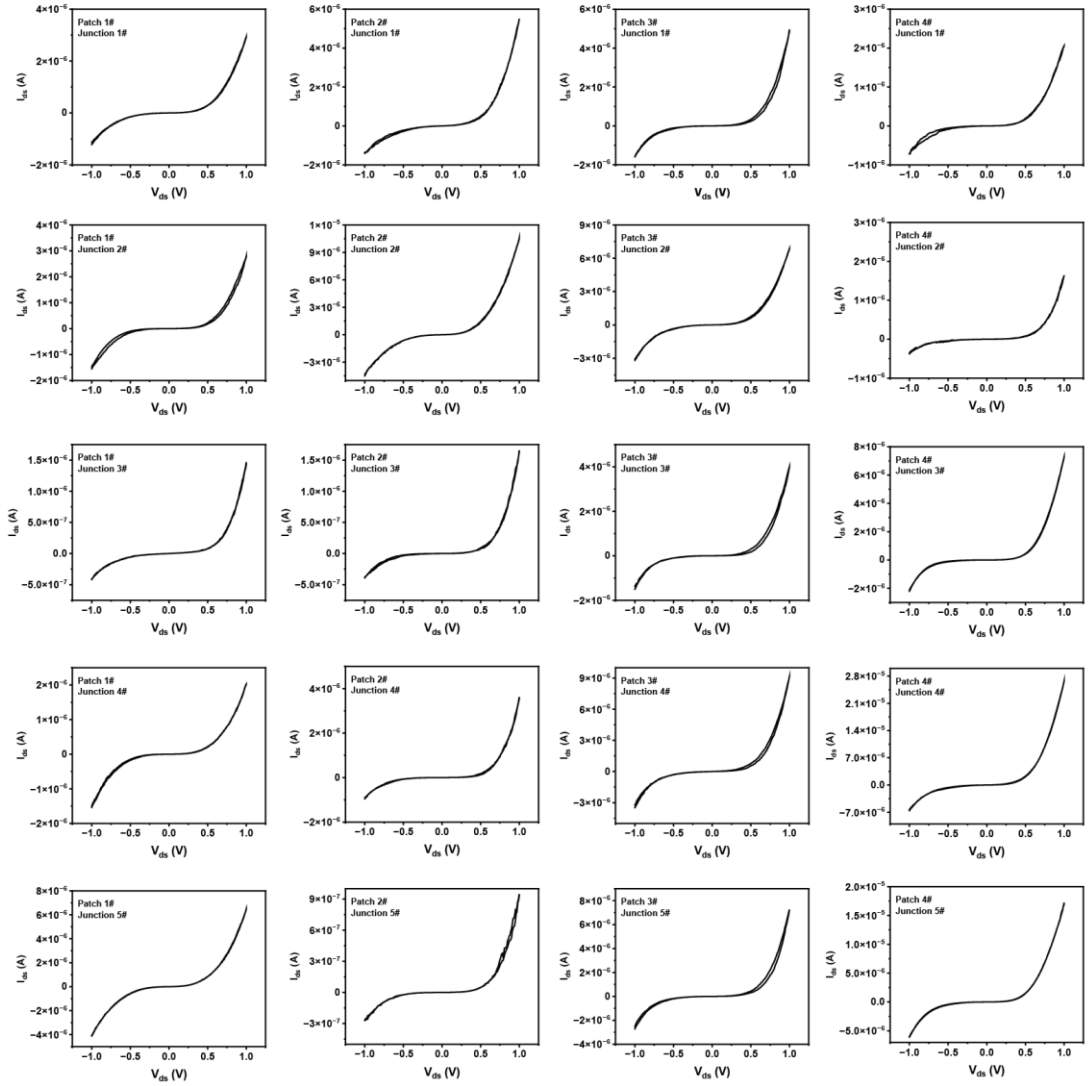

Supplementary Fig. 29 Twenty representative individual I_{ds}-V_{ds} curves of working junctions from 4 patches.

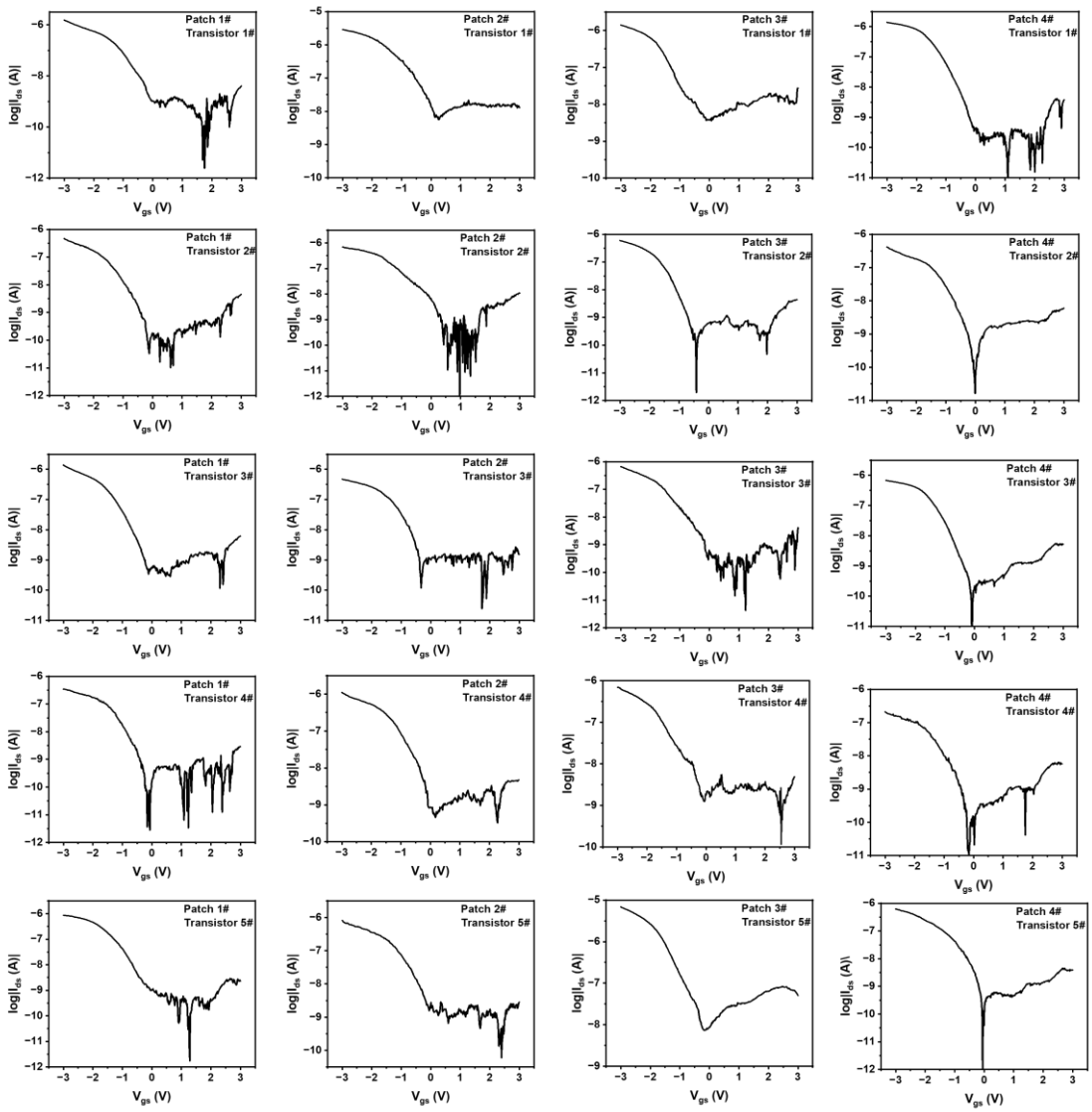

Supplementary Fig. 30 Twenty representative individual transfer characteristics of HOMO-type molecular transistors from 4 patches.

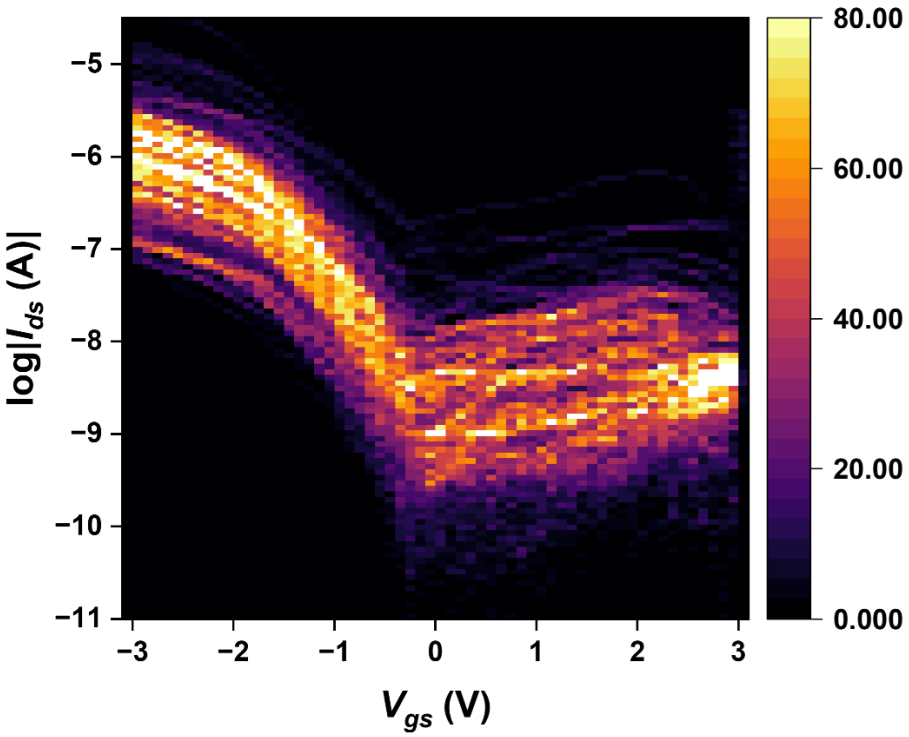

Supplementary Fig. 31 Heatmap of transfer characteristics collected from 200 HOMO-type molecular transistors.

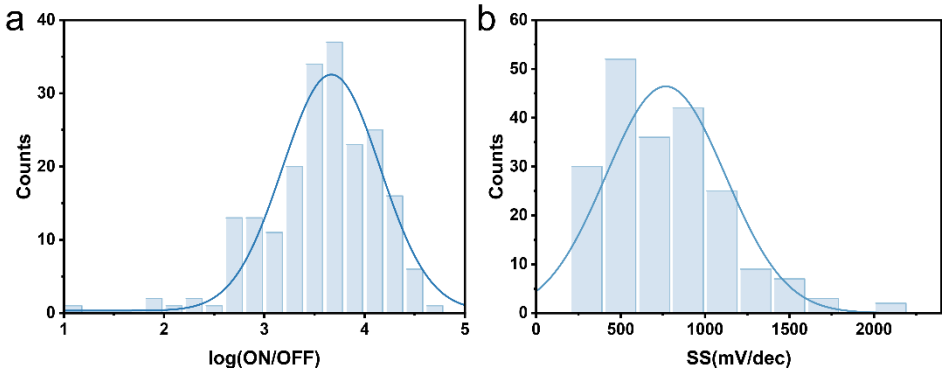

Supplementary Fig. 32 a. Distribution of ON/OFF ratios corresponding to transfer characteristic curves (V_(ds) = 0.1 V) of 200 randomly selected HOMO-type molecular transistors. ON/OFF = 4,660; σ log(ON/OFF) = 0.49. b. Subthreshold swing distribution for 200 randomly selected HOMO-type molecular transistors, showing 767 ± 354 mV/dec.

Supplementary Note 4.8 Wiring diagrams for molecular logic gates

The implementation of molecular logic gates requires external load resistors of 1 MΩ for proper operation. Supplementary Fig. 33 demonstrates the circuit configurations for NOT, NOR, and NAND gates.

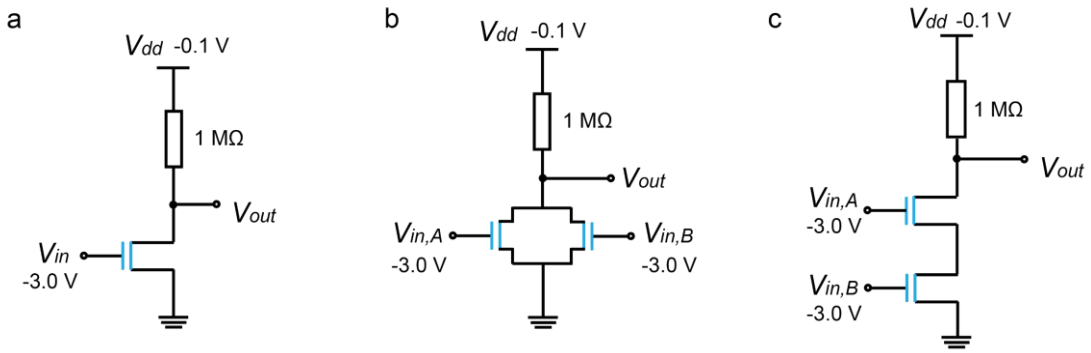

Supplementary Fig. 33 The wiring diagrams for (a) NOT, (b) NOR and (c) NAND gates.

Supplementary Note 4.9 Lifetime of HOMO-type transistor

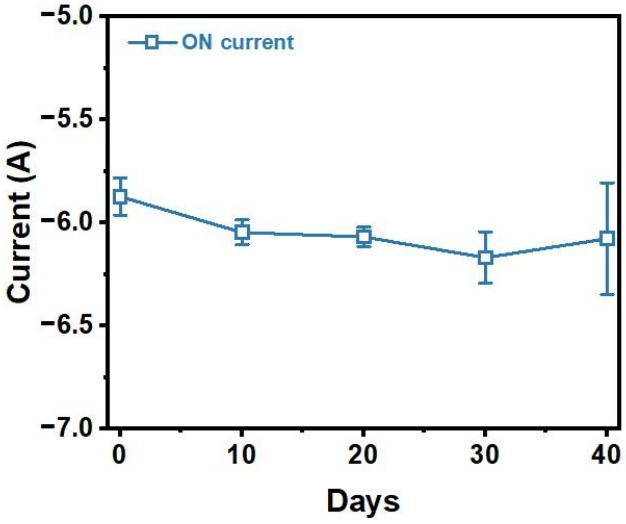

Supplementary Fig. 34 The ON current of HOMO-type transistors stored in air. Error bars represent standard deviation (SD).

Supplementary Note 5. DFT calculation of molecular transistors

Supplementary Note 5.1 Molecular frontier orbitals of exTTF-SH and C_{60}-SH

The molecular orbitals involved in charge transport through the molecular transistors are the HOMO for exTTF-SH and the LUMO for C_{60}-SH. Computational results indicate that the corresponding molecular frontier orbitals are localized within the functional groups of the molecules, spatially separated from the anchoring groups by the molecular backbone. This design strategy may effectively minimize hybridization with the bottom electrodes.

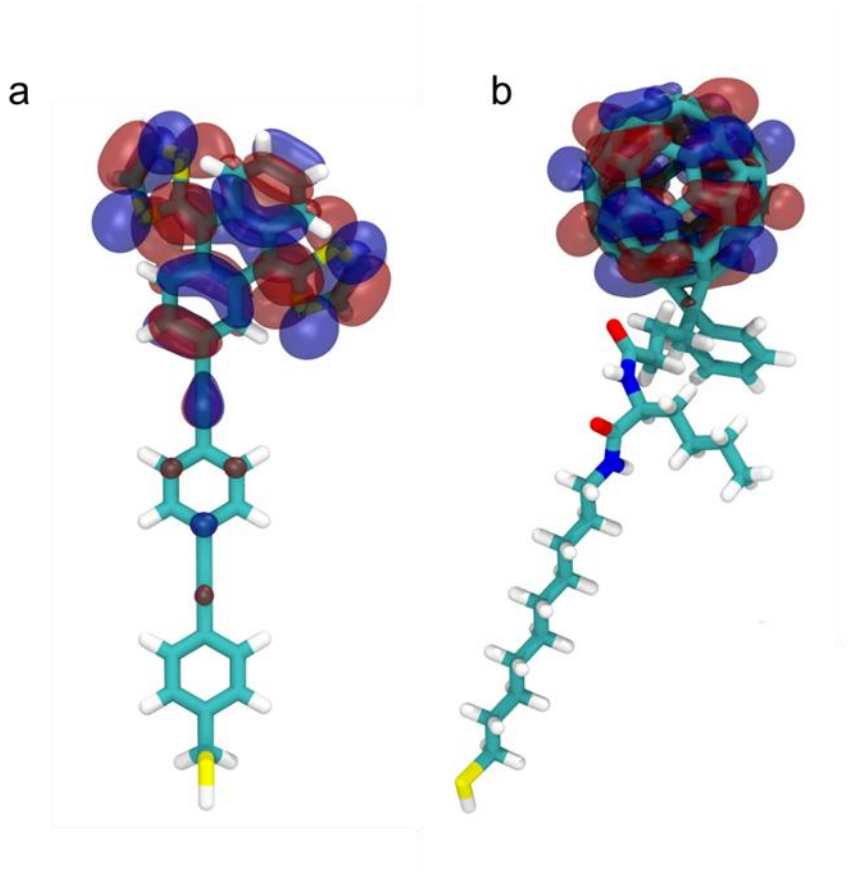

Supplementary Fig. 35 The calculated molecular frontier orbitals for (a) HOMO of exTTF-SH and (b) LUMO of C_{60}-SH.

Supplementary Note 5.2 Model of two-terminal molecular junctions

The DFTB modelling-predicted Au-S-C_{60} current is much lower than Au-S-exTTF, contrary to the experimental data. To check the cause of this discrepancy, additional calculations were carried out using full DFT with SIESTA[25,26] and its associate transport software TBTrans[27,28]. The GGA functional PBE[29] was used with a double-zeta basis set and optimized norm-conserving Vanderbilt pseudopotentials[30, 31] provided in the PseudoDojo library[32,33,34]. The DFT results, shown in Supplementary Fig. 37, are similar in amplitude to those obtained using DFTB. This shows that the computational method does not change the predicted ranking of the molecules in terms conductivity. Thus, this discrepancy likely stems from the absence of supramolecular packing in the model[35,36]. This is reflected in the position of the HOMO and LUMO displayed in Figure 1e. The predicted HOMO of exTTF is closer to the Fermi level than experimentally measured, and the predicted C_{60} LUMO is further from the Fermi level than experimentally measured. The experimental data, however, were obtained from SAM, not idealised single molecule, devices. Furthermore, the computational models are simple junctions, not transistors, which cannot be yet modelled with existing charge transport algorithms. The absence of the field effect may also contribute to the discrepancy between experiment and theory. However, our model shows, in line with the interpretation of experimental results, that the relative position with respect to the Fermi level of gold of the HOMO for p-type systems and of the LUMO for n-type governs the electron transport mechanism, and therefore the output current. The model thus predict that it is possible for gate voltage V_{gs} to shift the positions of the molecular orbitals and regulate the channel conductance, which guides the interpretation of the experimental electrical measurements.

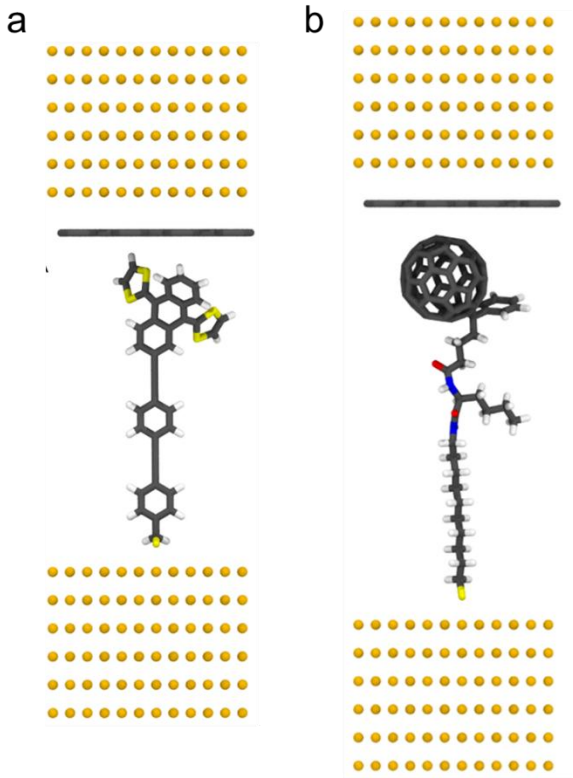

Supplementary Fig. 36 Representations of the two-terminal models for the (a) Au-S-exTTF//SLG and (b) Au-S-C_{60}//SLG junction

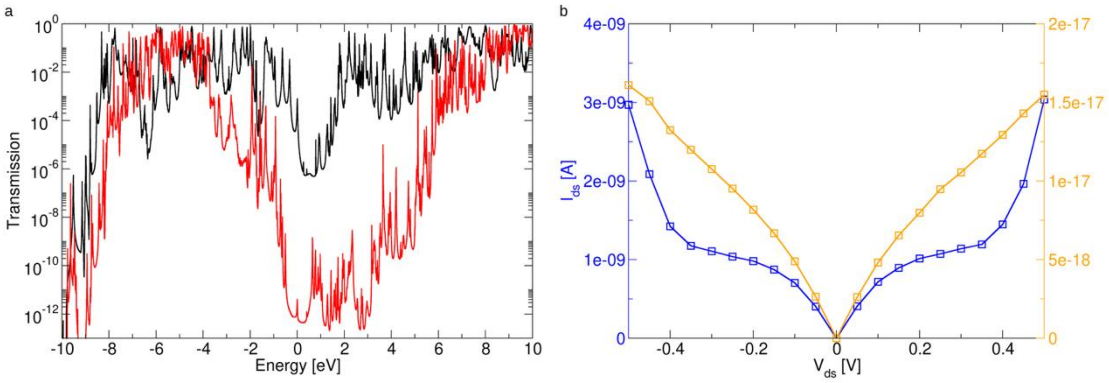

Supplementary Fig. 37 a) Transmissions functions for Au-S-exTTF//SLG (black) and Au-S-C_{60}//SLG (red) junction. b) *IV* plots for Au-S-exTTF//SLG (blue) and Au-S-C_{60}//SLG (orange) junction. DFT calculations were carried out with SIESTA[25,26], and transport calculations were performed with its companion software TBTRANS[27,28]. The PBE[29] functional was used with a double-zeta basis set. Pseudopotentials[30,31] were obtained from the PseudoDojo library[32,33,34].

References in supporting information

1. Lin, J. L. et al. Molecular diodes with tunable threshold voltage based on π-extended tetrathiafulvalene. *Adv. Mater. Interfaces* **9**, 2201238 (2022).
2. Yang, Z. et al. High performance mechano-optoelectronic molecular switch. *Nat. Commun.* **14**, 5639 (2023).
3. Chen, Z. et al. Quantum interference enhances the performance of single-molecule transistors. *Nat. Nanotechnol.* **19**, 986–992 (2024).
4. Meng, L. et al. Dual-gated single-molecule field-effect transistors beyond Moore's law. *Nat. Commun.* **13**, 1410 (2022).
5. Mentovich, E. D. et al. 1-Nanometer-sized active-channel molecular quantum-dot transistor. *Adv. Mater.* **22**, 2182–2186 (2010).
6. Limburg, B. et al. Anchor groups for graphene-porphyrin single-molecule transistors. *Adv. Funct. Mater.* **28**, 1803629 (2018).
7. Wang, X. et al. Electrostatic Fermi level tuning in large-scale self-assembled monolayers of oligo(phenylene-ethynylene) derivatives. *Nanoscale Horiz.* **7**, 1201–1209 (2022).
8. Xin, N. et al. Tuning charge transport in aromatic-ring single-molecule junctions via ionic-liquid gating. *Angew. Chem. Int. Ed.* **57**, 14026–14031 (2018).
9. Mentovich, E. D. et al. Large-scale fabrication of 4-nm-channel vertical protein-based ambipolar transistors. *Nano Lett.* **9**, 1296–1300 (2009).
10. Famili, M. et al. Self-assembled molecular-electronic films controlled by room temperature quantum interference. *Chem* **5**, 474–484 (2019).
11. Jia, C. et al. Quantum interference mediated vertical molecular tunneling transistors. *Sci. Adv.* **4**, eaat8237 (2018).
12. Lovat, G. et al. Room-temperature current blockade in atomically defined single-cluster junctions. *Nat. Nanotechnol.* **12**, 1050–1054 (2017).
13. Xu, B. et al. Large gate modulation in the current of a room temperature single molecule transistor. *J. Am. Chem. Soc.* **127**, 2386–2387 (2005).
14. Li, X. et al. Supramolecular transistors with quantum interference effect. *J. Am. Chem. Soc.* **145**, 21679–21686 (2023).
15. Yan, Z. et al. Single-molecule field effect and conductance switching driven by electric field and proton transfer. *Sci. Adv.* **8**, eabm3541 (2022).
16. Cao, Z. et al. Flexible crossbar molecular devices with patterned EGaIn top electrodes for integrated all-molecule-circuit implementation. *Adv. Mater.* **36**, 2406456 (2024).
17. Wan, A. et al. Arrays of high quality SAM-based junctions and their application in molecular diode based logic. *Nanoscale* **7**, 19547–19556 (2015).
18. Phan, T. L. et al. CNT-molecule-CNT (1D-0D-1D) van der Waals integration ferroelectric memory with 1-nm(2) junction area. *Nat. Commun.* **13**, 4556 (2022).
19. Han, Y. et al. Electric-field-driven dual-functional molecular switches in tunnel junctions. *Nat. Mater.* **19**, 843–848 (2020).
20. Green, J. E. et al. A 160-kilobit molecular electronic memory patterned at 10(11) bits per square centimetre. *Nature* **445**, 414–417 (2007).
21. Chen, N. et al. Extreme long-lifetime self-assembled monolayer for air-stable molecular junctions. *Sci. Adv.* **9**, eadh3412 (2023).
22. Qiu, L. et al. Rectification of current responds to incorporation of fullerenes into mixed-monolayers of alkanethiolates in tunneling junctions. *Chem. Sci.* **8**, 2365–2372 (2017).
23. Yuan, L. et al. Transition from direct to inverted charge transport Marcus regions in molecular junctions via molecular orbital gating. *Nat. Nanotechnol.* **13**, 322–329 (2018).
24. Wang, H. et al. Photophysical and Electronic Properties of Five PCBM-like C60 Derivatives: Spectral and Quantum Chemical View. *J. Phys. Chem. A* **116**, 255–262 (2012).
25. García, A. et al. Siesta: Recent developments and applications. *J. Chem. Phys.* **152**, 204108 (2020).
26. Soler, J. M. et al. The SIESTA method for ab initio order-N materials simulation. *J. Phys.: Condens. Matter* **14**, 2745 (2002).
27. Brandbyge, M. et al. Density-functional method for nonequilibrium electron

transport. *Phys. Rev. B* **65**, 165401 (2002).
28. Papior, N. et al. Improvements on non-equilibrium and transport Green function techniques: The next-generation transiesta. *Comput. Phys. Commun.* **212**, 8–24 (2017).
29. Perdew, J. P., Burke, K. & Ernzerhof, M. Generalized Gradient Approximation Made Simple. *Phys. Rev. Lett.* **77**, 3865–3868 (1996).
30. Hamann, D. R. Optimized norm-conserving Vanderbilt pseudopotentials. *Phys. Rev. B* **88**, 085117 (2013).
31. García, A. et al. The psml format and library for norm-conserving pseudopotential data curation and interoperability. *Comput. Phys. Commun.* **227**, 51–71 (2018).
32. van Setten, M. J. et al. The PseudoDojo: Training and grading a 85 element optimized norm-conserving pseudopotential table. *Comput. Phys. Commun.* **226**, 39–54 (2018).
33. Lejaeghere, K. et al. Reproducibility in density functional theory calculations of solids. *Science* **351**, aad3000 (2016).
34. Garrity, K. F. et al. Pseudopotentials for high-throughput DFT calculations. *Comput. Mater. Sci.* **81**, 446–452 (2014).
35. Hyllested, L. O. H., Prestholm, I. & Solomon, G. C. Intermolecular Interactions and Quantum Interference Effects in Molecular Junctions. *ACS Nanosci. Au* **4**, 426–434 (2024).
36. Garrigues, A. R. et al. Electrostatic control over temperature-dependent tunnelling across a single-molecule junction. *Nat. Commun.* **7**, 11595 (2016).